Chemie der Erde 72 (2012) 1–23

Contents lists available at SciVerse ScienceDirect

Chemie der Erde

journal homepage: www.elsevier.de/chemer

Invited review

Tooting crater: Geology and geomorphology of the archetype large, fresh, impact crater on Mars

Peter J. Mouginis-Mark*, Joseph M. Boyce

Hawaii Institute Geophysics and Planetology, School of Ocean Earth Science and Technology, University of Hawaii, Honolulu, HI 96822, USA

ARTICLE INFO

Article history:
Received 17 August 2011
Accepted 1 December 2011

Keywords:
Mars
Tooting crater
Impact cratering
Geomorphology
HiRISE

ABSTRACT

The 27.2 km diameter Tooting crater is the best preserved young impact crater of its size on Mars. It offers an unprecedented opportunity to study impact-related phenomena as well the geology of the crust in the Amazonis Planitia region of Mars. For example, the nearly pristine condition enables the partial reconstruction of the sequence of events for crater formation, as well as facilitates a comparison to deposits seen at the Ries crater in Germany. High-resolution images taken by the High Resolution Imaging Science Experiment (HiRISE) and Context Camera (CTX) on the Mars Reconnaissance Orbiter spacecraft have revealed a wealth of information on the distribution of features within the crater and beyond the rim: a large central peak, pitted material on the floor and terrace blocks, lobate flows interpreted to be sediment flows, impact melt sheets, four discrete layers of ejecta, and an asymmetric secondary crater field. Topographic data derived from the Mars Orbiter Laser Altimeter (MOLA) and stereo HiRISE and CTX images show that the central peak is ~1100 m high, the lowest point of the crater floor is 1274 m below the highest part of the rim, and the crater rim has ~600 m of variability around its perimeter. Layering within the cavity walls indicates ~260 m of structural uplift of the target material, which constitutes ~35% of the total relief of the rim. Abundant evidence is found for water flowing down the cavity walls, and on the surface of the ejecta layers, both of which took place sometime after the impact event. Thickness measurements of the ejecta layers reveal that the continuous blanket is remarkably thin (~3–5 m) in some places, and that the distal ramparts may be ~60 m high. Crater counts made on the ejecta layers indicate a model age of <3 Ma for the formation of Tooting crater, and that the target rocks have a model age of ~240–375 Ma. It is therefore possible that this may be the source of certain basaltic shergottite meteorites ejected at ~2.8 Ma that have crystallization ages which are comparable to those of the basaltic lava flows that formed the target materials for this impact event. The geology and geomorphology of Tooting crater may help in the interpretation of older large impact craters on Mars, as well as the potential role of target volatiles in the impact cratering process.

1. Introduction

Impact craters on all planetary bodies provide crucial information on the subsurface structure of the target material, as well as insights into the cratering process (Melosh, 1989). In the case of Mars, the three-dimensional structure of a crater is particularly important as it may provide evidence for spatial or temporal variations in the distribution of volatiles at depth at the time when the crater formed. However, one particularly challenging task has been to determine the inter-play between the products of the cratering event (impact melt, ejecta, and the sediments that are produced during the impact event), and the physical state (solid or liquid) of any volatiles that may have existed within the target rock at the time of crater formation (Kieffer and Simonds, 1980; Osinski et al., 2008). The identification of the duration and relative timing of the events during the formation of the crater is also important, including the formation of impact melt and sediment flows (Morris et al., 2010), ejecta emplacement (Barnouin-Jha et al., 2005; Baloga et al., 2005), and the hydrothermal properties of the crater cavity (Abramov and King, 2005).

Since the earliest days of the Viking Orbiter missions, analysis of the lobate deposits surrounding many Martian impact craters has suggested the presence of water or ice within the top kilometer or more of the crust at the time of crater formation (Head and Roth, 1976; Carr et al., 1977; Gault and Greeley, 1978; Mouginis-Mark, 1979, 1987). The terms "rampart crater" and "multi-layered ejecta craters" have been used to describe these craters (Mouginis-Mark, 1978; Barlow et al., 2000). Details of ejecta emplacement have also been studied, particularly in the context of understanding the rheology of the flows and the flow process (Woronow, 1981; Baloga

* Corresponding author. Tel.: +1 808 956 8760; fax: +1 808 956 3188.
E-mail address: pmm@hawaii.edu (P.J. Mouginis-Mark).

0009-2819/$ – see front matter © 2011 Elsevier GmbH. All rights reserved.
doi:10.1016/j.chemer.2011.12.001

et al., 2005), and the possible insights that the physical and spectral properties of the ejecta blankets may provide about the target materials (Ivanov, 1996; Stewart and Valiant, 2006; Baratoux et al., 2007; Black and Stewart, 2008).

By studying the best preserved examples of Martian impact craters, several questions can be addressed that are of importance for the analysis of the thousands of older, morphologically-degraded craters. For example, are the fluidized ejecta patterns seen around most fresh Martian craters due to impact into subsurface volatile reservoirs, to the interaction with the thin Martian atmosphere, or to a combination of these processes? Two models exist to explain the origin of the lobate ejecta morphologies: impact into, and subsequent vaporization of, subsurface volatiles (Carr et al., 1977; Gault and Greeley, 1978; Mouginis-Mark, 1979, 1981) or ejecta entrainment into the thin Martian atmosphere (Schultz and Gault, 1979; Barnouin-Jha and Schultz, 1998). Analysis of the freshest craters on Mars may permit the unraveling of the role of the target properties in the emplacement of the ejecta blanket. In this instance, near-pristine crater morphology may help to identify regions that have contained, or still contain, volatiles. Differences in geologic materials may also affect the formation and distribution of specific types of impact craters (Mouginis-Mark, 1979), in part controlling the size of central peaks and specific flow patterns within the ejecta layers. It is possible that the morphometric properties of Martian impact craters vary with latitude, terrain, or elevation, either because of spatial variations in the distribution of volatiles, or due to different mechanical properties of the target rocks; detailed analysis of the distribution of these craters qualitatively confirm these spatial variations (Mouginis-Mark, 1979; Barlow and Perez, 2003), but to date no detailed quantitative analysis of the morphology of individual impact craters has been conducted.

It has been postulated that volatiles lay within target rocks when most impact craters formed on Mars (Carr et al., 1977; Mouginis-Mark, 1987; Barlow and Perez, 2003; Osinski, 2006; Black and Stewart, 2008). Many of the lobate ejecta layers from these craters have been hypothesized to have been mobilized by water or ice contained within the ejecta during the excavation of the crater cavity (Greeley et al., 1980). But little evidence has to date been presented to confirm that the top-most kilometer or two of the target rock contained liquid water or ice, particularly in the mid-latitudes, although water ice has been found at a few centimeters depth at the Phoenix landing site (Mellon et al., 2009) and detected at very shallow depth (<2 m) from small craters that have formed during the past few years (Byrne et al., 2009).

Few large (>25 km diameter) impact craters are sufficiently young that details of the original morphology and geometry of the crater can confidently be determined. In the case of the Moon, the 92 km diameter crater Copernicus has often been taken as an archetypical fresh crater, with detailed mapping of the crater cavity (Howard, 1975; Howard and Wilshire, 1975) revealing considerable information on the structure of the crater, as well as the distribution of impact melt. On Mars, Tooting crater (23°15′N, 207°45′E; Fig. 1) is one of the very small group of very fresh large impact craters (Mouginis-Mark and Garbeil, 2007; Hartmann et al., 2010), has a mean diameter of 27.2 km, and has a wide array of geomorphic units preserved on the crater rim, inner wall units, and floor. These units include probable impact melt sheets and sediment flows (Morris et al., 2010), and extensive areas of pitted terrain on the floor (Mouginis-Mark and Garbeil, 2007). The origin of the sediment flows in Martian craters is enigmatic, with possible origins including either dry or wet sediment flows (Lanza et al., 2010; Morris et al., 2010).

In this review article, we will demonstrate that the materials surrounding Tooting crater reveal a wide diversity of emplacement processes, including fluid flow (i.e., water leaking out of the crater cavity) from the near-rim deposits and diverse styles of surface flow of the ejecta layers. (*Note*: in addition to the figures reproduced in this printed form, additional illustrations are provided in the on-line supplement, and are denoted as "Fig. S" in the text. The locations of all of the supplemental figures are provided in Figs. S1 and S2). The distal ramparts of these ejecta layers are remarkably well preserved, and there is an abundance of secondary

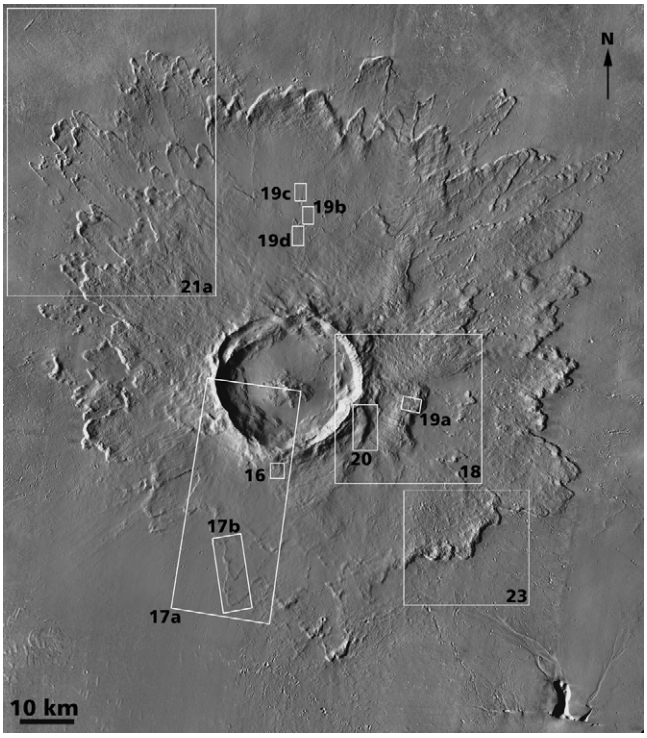

Fig. 1. (a) Overview of Tooting crater, showing the locations of Figs. 16–21 and 23. Mosaic of THEMIS VIS images, constructed by Ryan Luk of Arizona State University. (b) Geologic map of Tooting crater, mapped at a scale of 1:200,000, by Mouginis-Mark (submitted for publication).

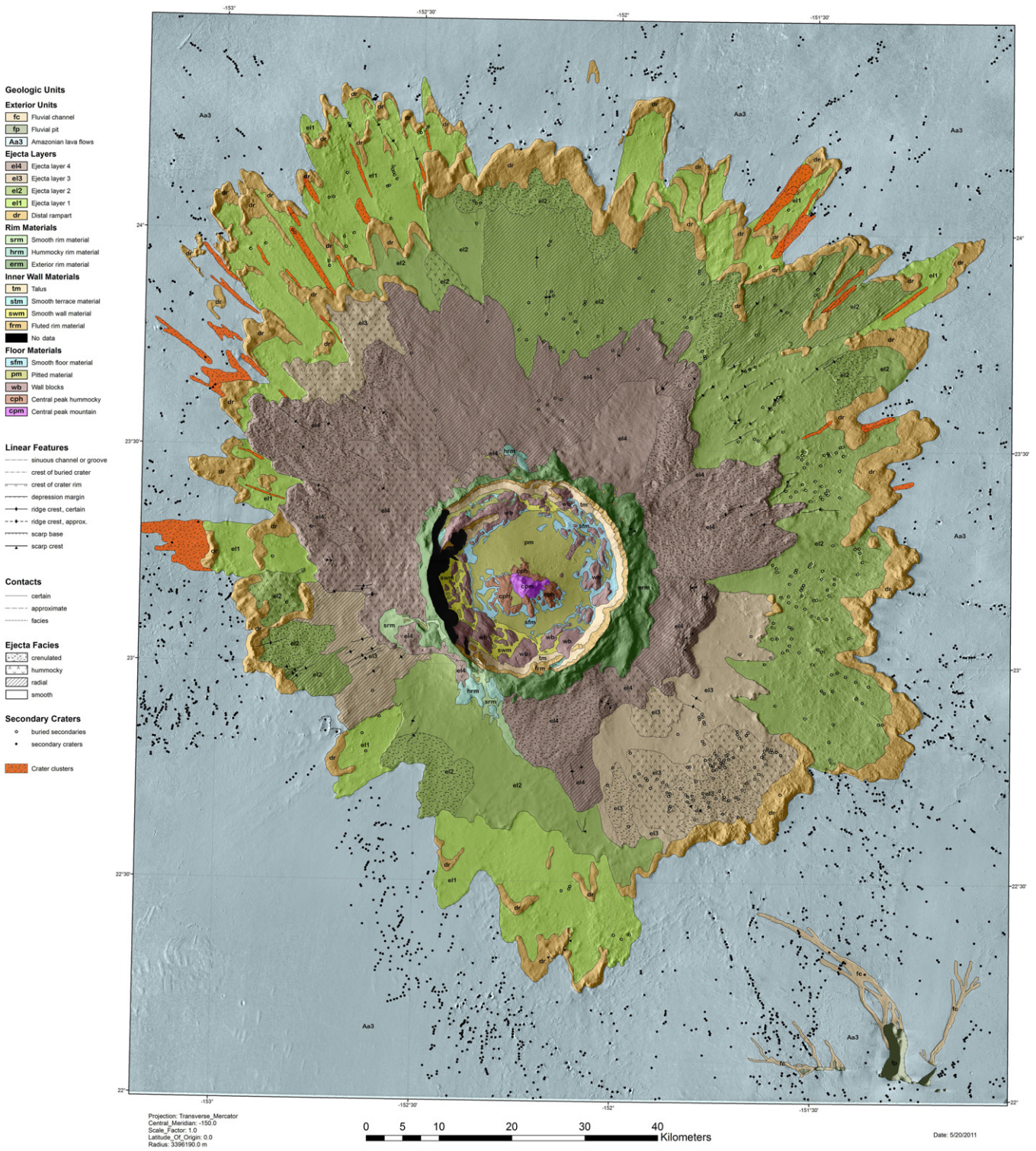

Fig. 1. (*continued.*)

craters that extend to radial distances in excess of 540 km (~40 crater radii) from the rim crest. Through the efforts of the High Resolution Imaging Science Experiment (HiRISE), Context Camera (CTX), and Thermal Emission Imaging System (THEMIS) Imaging Teams, the crater has been extensively imaged, with almost complete coverage of the crater cavity obtained at a spatial resolution of 25 cm/pixel. We present here many new observations based upon these images, which have permitted formal geologic mapping of the crater cavity and ejecta layers at a scale of 1:200,000 (Mouginis-Mark, submitted for publication), as well as preliminary mapping at scales of 1:5000, 1:10,000 and 1:25,000. These observations include the identification of pitted terrain on the floor and terraces, abundant evidence for the flow of water soon after the impact event, and the production of impact melt. Topographic data, derived from the Mars Orbiter Laser Altimeter (MOLA) and digital elevation models (DEMs) from stereo images, provide new insights into the thickness of the ejecta blanket, the magnitude of structural uplift of the rim, and the geometry of the distal ramparts.

Collectively, these observations enable older impact craters on Mars to be further interpreted in the context of impact-induced hydrothermal activity (Rathbun and Squyres, 2002; Abramov and King, 2005; Barnhart et al., 2010) and the modification of the crater cavity. We also briefly consider the idea that this crater may be a source of some of the SNC meteorites (Wood and Ashwal, 1981; Mouginis-Mark et al., 1992; Treiman, 1995; McSween et al., 1996; Kring et al., 2003; Hamilton et al., 2003; Tornabene et al., 2006) and compare its morphology to that of the terrestrial Ries impact crater (Hörz et al., 1983; Osinski et al., 2004; Kenkmann and Schonian, 2006). We conclude with a discussion of how the interpretation of older impact craters on Mars may be improved by this greater knowledge of the pristine geology and geometry.

2. Geographic setting and crater geometry

Tooting crater was formally named in 2005 by the International Astronomical Union. This name derives from the town of Tooting in South London, England (where the lead author of this paper was born). Tooting was first described in a Saxon charter dated A.D. 675, when it was called "Totinge". It was also mentioned in the Domesday Book in 1086. "Tooting" comes from the name of the Saxon Tota and follows the old English custom of adding "ing" (which means "the people who lived at") to the person's name. Thus "Tooting" literally means "The home of Tota's people".

Tooting crater (23°10′N, −152°10′E) formed on virtually flat lava flows within Amazonis Planitia (Fig. 2) where there appear to have been no other major topographic features prior to the impact. The crater formed in an area ~185 × 135 km in size that is at an elevation between −3870 m and −3874 m relative to the MOLA Mars datum (Smith et al., 1999). This fortuitous situation (i.e., bland, horizontal target) means that the geometry of the crater and the thickness of the ejecta blanket can be accurately determined by subtracting the mean elevation of the surrounding landscape (−3872 m) from the individual MOLA measurements across the crater. Thus, for the first time, it is possible to measure the amount of structural uplift of the pre-existing target material within the walls of the crater cavity, estimate the absolute ejecta thicknesses with reasonable accuracy for a fresh multi-layered impact crater on Mars, as well as measure the radial decrease of thickness as a function of distance away from the rim crest (Mouginis-Mark and Garbeil, 2007).

Tooting crater (Fig. 3) is very young in comparison to other morphologically fresh large craters on Mars such as Hale crater (~120 × 150 km diameter) (Jones et al., 2011) and appears to be comparable in age to the smaller (~10 km diameter) crater Zunil (McEwen et al., 2005). Mouginis-Mark and Garbeil (2007) inspected 30 THEMIS VIS images and found a total of 13 superposed impact craters in the diameter range 54–234 m (i.e., 3–13 THEMIS pixels) on the ejecta blanket, which has an area of ~8120 km^2. Using the final 2004 iteration of the Martian crater-count isochron (see Table 2 in Hartmann, 2005), this gave an approximate age that is most likely less than 2 Ma. We have now performed more detailed crater counts both on the ejecta layers (using HiRISE data) and on the surrounding Amazonian-age lava flows (using CTX data) to derive better age estimates. We mapped all impact craters in an area of 500 km^2 using CTX image P22_009687_2004_XN_20N155W. A total of 398 craters in the diameter range 60–1098 m were identified. For these ejecta layers, mapping was conducted on HiRISE frames PSP_007116_2035, PSP_007116_2035 and ESP_017625_2040. The area mapped was 36.887 km^2. A total of 206 craters in the diameter range 10.0–60.0 m were identified. The cumulative crater counts (and associated error bars) for the ejecta blanket are presented in Fig. 4, and the locations where these crater counts were collected are shown in Fig. S3. Based upon the modeling of Hartmann and Neukum (2001) and Ivanov (2001), the size-frequency curves

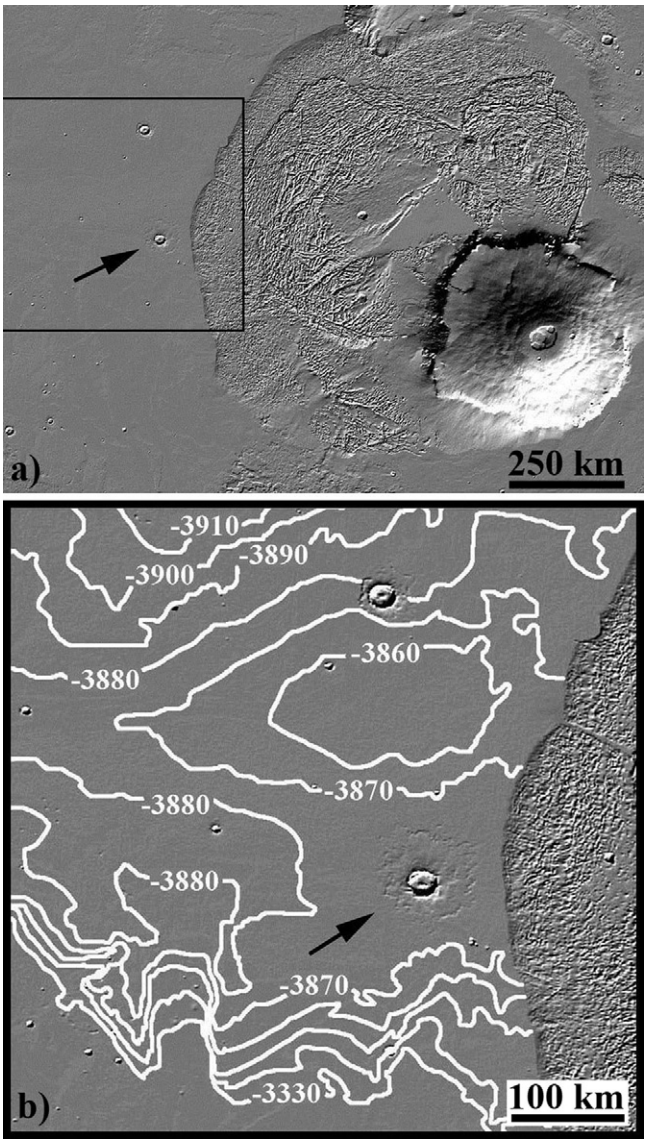

Fig. 2. Images showing the location of Tooting crater to the west of Olympus Mons volcano (a). Black box delineates location of lower image. In (b), the very flat terrain surrounding the crater can be seen. Arrows point to Tooting crater. Contours give elevations in meters referenced to the MOLA datum of Smith et al., 1999. Base images are shaded relief renditions of MOLA 128th-degree digital elevation model, with the illumination from the south.

indicate an age of ~2.9 Ma ± 0.3 Ma for Tooting crater, and 240–375 Ma for the pre-impact surface (i.e., the Late Amazonian-age lava flows surrounding the crater; Scott and Tanaka, 1986). This target material is, therefore, well within the age range (from <100 Ma to a few 100 Ma) of volcanic surfaces identified by Hauber et al. (2011) that lie to the east of Olympus Mons.

Hartmann et al. (2010) gave an older age (of at least a few million years) by counting craters on a small segment of one terrace block and unspecified areas of the ejecta blanket. This block does not, however, mimic the crater distribution observed upon the much larger total surface area, and widely distributed sample areas of undisturbed ejecta deposits identified in Fig. S3. We therefore believe that the ejecta layers are much more representative and far less cratered than the small areas studied by Hartmann et al. (2010), so that the age of Tooting crater is much more consistent with an age of ~2.9 Ma.

Using individual MOLA shots co-registered with THEMIS VIS images, Mouginis-Mark and Garbeil (2007) were able to measure

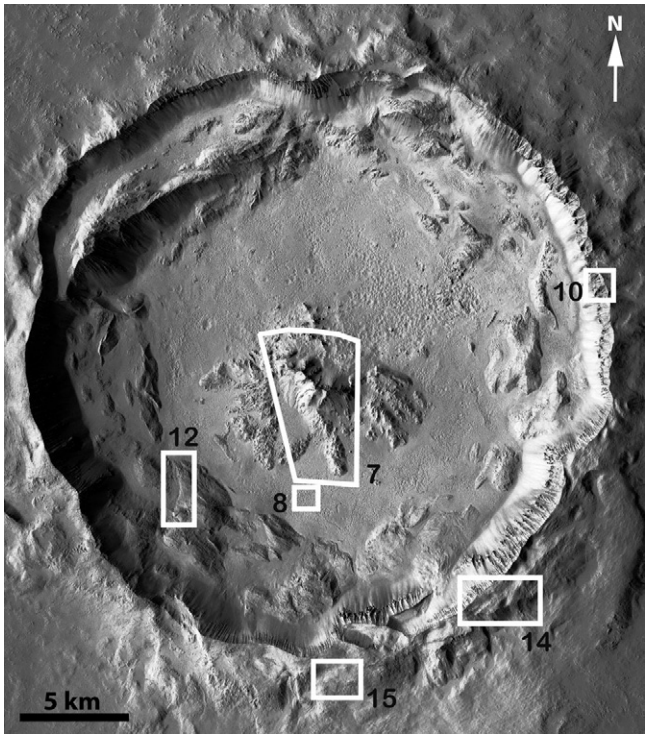

Fig. 3. Close-up view of the cavity, showing the locations of Figs. 7, 8, 10, 12, 14 and 15. CTX image P01_001538_2035.

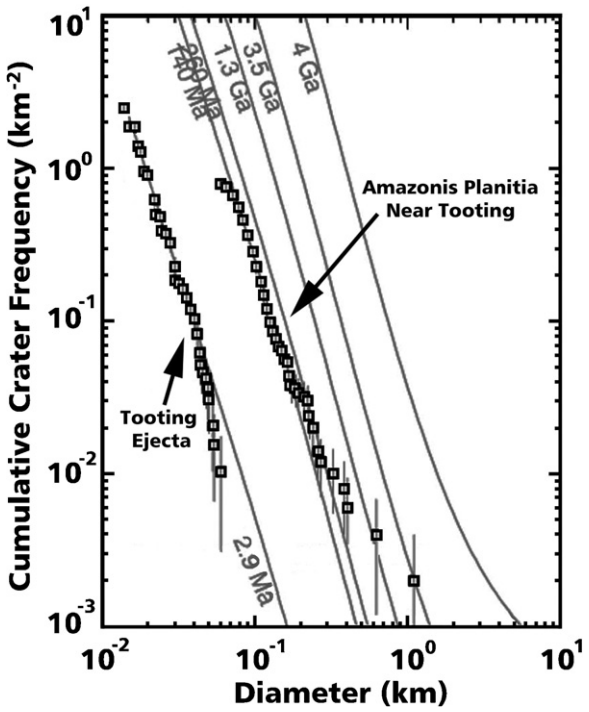

Fig. 4. Cumulative size/frequency distribution of small craters on several segments of the ejecta layers. Also shown are crater counts for the lava flows to the SW of the crater, beyond any of the secondary craters produced by the ejecta. Error bars expressed as the square root of the number of craters measured in each diameter range. See Fig. S2 for locations of the areas measured.

the depth, rim height, and azimuthal variation in rim height. Since this study, we have produced a DEM from a stereo pair of CTX images (frame numbers P01_001538_2035_XI_23N152W and P03_002158_2034_XI_23N152W) that allows a more complete analysis of the geometry of the crater (Figs. 5 and S4), as well as an investigation of the rim crest topography (Fig. 6). The cross-section through the cavity (Fig. 5) reveals that the lowest point on the southern floor is at −5146 m, and the lowest point on the northern floor is at −4954 m, relative to the MOLA datum of Smith et al. (1999). These values are lower than the comparable elevations identified by Mouginis-Mark and Garbeil (2007) from individual MOLA profiles that cross the crater floor (i.e., −5125 m and −4934 m, respectively), and mean that the crater floor is 1274 m below the surrounding terrain in the southern floor, and 1082 m below the surroundings in the northern floor. There is a terrace bench on the left side of the profile, which has a "rim" that is 290 m high. This terrace bench is ~865 m above the northern crater floor and the southern floor is ~190 m below the northern floor.

Using the CTX DEM, we find that the minimum rim elevation is 347 m, and the maximum elevation is 951 m, which exceed the earlier minimum and maximum values (386 m and 893 m, respectively) estimated from MOLA shots taken across the rim crest (Mouginis-Mark and Garbeil, 2007). Taking 27.2 km as the diameter, the rim height/crater diameter ratio of the crater therefore

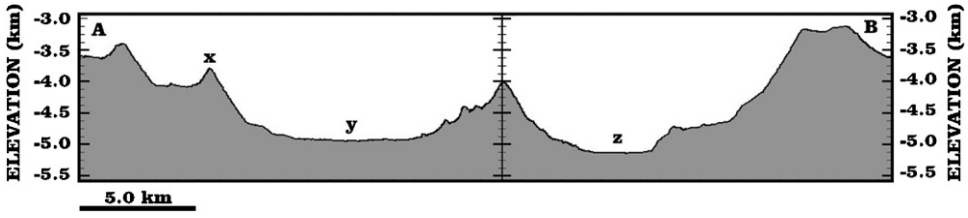

Fig. 5. Topographic profile A to B through the cavity of Tooting crater, derived from CTX DEM (see Fig. S2 for profile location). Note the terrace bench on the left side of the profile, which has a "rim" that is 290 m high (at "x"). This terrace bench is ~865 m above the northern crater floor ("y"). Also note that the southern floor ("z") is ~190 m below the northern floor. Vertical exaggeration is 2.6. Elevation is relative to the MOLA datum of Smith et al. (1999).

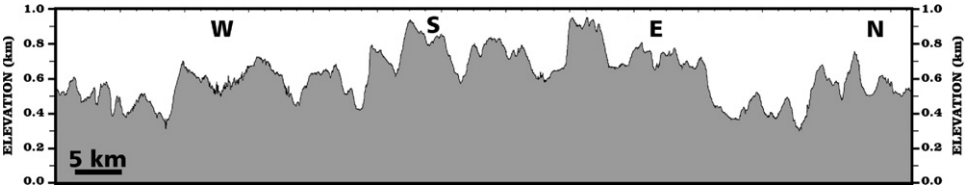

Fig. 6. Topography around the rim crest. Elevations are relative to the surrounding terrain, which is at an elevation of −3872 m relative to the MOLA datum of Smith et al. (1999). Compass bearings indicated by "W" (west), "S" (south), "E" (east) and "N" (north). Vertical exaggeration is ~18.7×.

varies from 0.013 to 0.039. The CTX DEM confirms that the southern and southeastern segments of the rim have the highest elevations and the lowest points are on the northwestern rim. The maximum depth/diameter ratio, as measured from the highest point on the rim to the lowest point of the floor, is ~0.082. The minimum depth/diameter ratio is 0.039.

3. Geology of Tooting crater

Through the collection of almost complete HiRISE (25 cm/pixel) and CTX (6 m/pixel) image coverage, it has been possible to study the morphology of the crater and its ejecta blanket at an unprecedented level. Very few other large impact craters on Mars have been imaged to this extent. The crater Zunil (10.1 km diameter) is an exception but, because of its smaller size, it does not display a similar wide diversity of geologic units; analysis of Zunil crater has focused on the distribution of the secondary craters produced during the impact event (Tornabene et al., 2006; Preblich et al., 2007). Williams and Malin (2008) have conducted a detailed analysis of the sub-kilometer-scale fans in Mojave crater (60 km diameter), and Jones et al. (2011) have investigated the ejecta blanket of Hale crater (125 × 150 km diameter) to try to determine if the impact event took place in an ice-rich crust. In none of these other investigations have both the interior and exterior deposits for the same crater been studied in detail.

Complete HiRISE coverage of the cavity permits us to produce a new geologic map (Fig. 1b) that allows the identification of many morphological features not previously documented on Mars, and features that have been speculated to exist based upon lower spatial resolution images of more degraded craters. Unfortunately, Tooting crater is located in a region of Mars that is mantled by an extensive layer of dust (Mellon et al., 2000; Ruff and Christensen, 2002). No information is available on the thickness of the dust layer, but it is sufficient to preclude any spectral analysis of the rocks using either THEMIS infrared data, or observations from the Compact Reconnaissance Imaging Spectrometer (CRISM). In this section we identify the startling diversity of these features, focusing upon the central peak complex, pitted material on the floor and terraces, the cavity wall, the rim units, and the proximal ejecta blanket within 0.2 crater radii from the rim crest.

3.1. Central peak complex

Tooting crater has a large central peak (Figs. 3 and 7), that measures ~10,630 m (E–W) and 8315 m (N–S), and has a surface area of 37.6 km^2. The HiRISE DEM reveals that the highest point on the peak is 1110 m above the surrounding floor material, or 119 m below the pre-existing level of the target material and 768 m below the average rim crest elevation. These dimensions give a peak height-to-crater-diameter ratio of 0.041, and an average height-to-base ratio of 0.117. There are two strikingly different morphologic components to the peak (Fig. S5): (1) a steep-sided high central mountain with exposed layering at the peak crest, and scree slopes on the middle and lower flanks; and (2) a lower-relief, hummocky component that occurs both as extensions of the central peak mountain and as outliers of material that appear to be partially buried by floor materials.

Central peaks in impact craters are interpreted to be uplifted materials from the pre-impact surface (Melosh, 1989, p. 136), and are composed of deformed and fractured rocks that originally underlay the transient crater. In the case of fresh lunar craters, the peaks often have compositions consistent with materials that originated from the lower crust (Pieters, 1982; Wieczorek and Zuber, 2001; Cahill et al., 2009). HiRISE images of the peak show that the central part of the peak is layered with units that could be pre-impact lava flows (Fig. S6). Using the relationship for structural uplift (SU) and crater diameter (D), SU = 0.086$D^{1.03}$ (Cintala and Grieve, 1998), would suggest that the central peak may have been uplifted as much as 2.85 km; the fact that we see layering within the peak suggests that the stack of lava flows within Amazonia Planitia is at least ~3 km thick, which is much thicker than can be measured by sounding radar measurements in this area (Campbell et al., 2008). Little evidence for the extensive deformation that is seen within peak complexes in terrestrial craters (Ferriere et al., 2008) can be found.

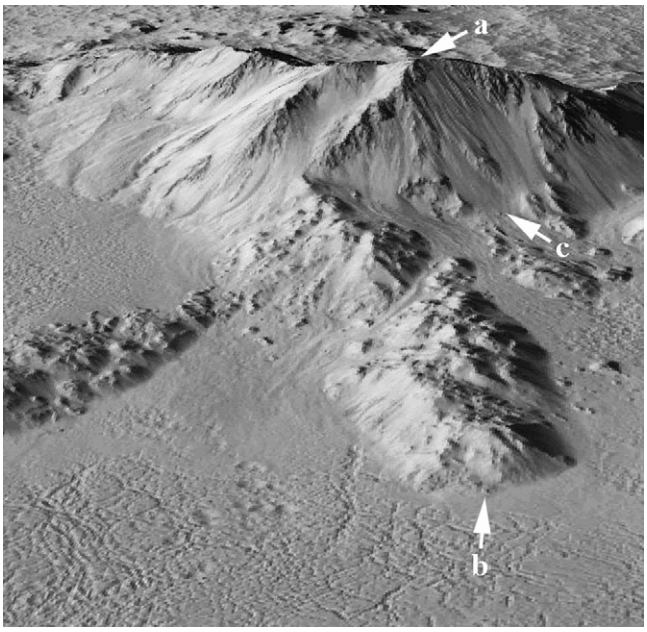

Fig. 7. Oblique view from above the south rim, looking north towards the central peak complex. Point "a" is at an elevation of −3991 m relative to Mars datum (Smith et al., 1999), and point "b" is at −5101 m. The width of this part of the hummocky peak material is ~1030 m wide. The foot of the scree slope ("c") is at −4785 m. Notice the fractured and pitted terrain in the foreground. Talus drapes much of the higher parts of the peak. Part of HiRISE image PSP_002158_2035.

The western side of the peak complex is unusual because it displays examples of lobate flows that emanate from the peak material (Fig. S7). To our knowledge, this type of flow has not yet been identified from any other central peak within a Martian impact crater. The flows are ~50 m wide and up to 2.4 km long, have narrow (<5 m wide) raised lateral levees, and occur on slopes of ~6–8°. No obvious source region for these flows can be identified, nor is there any clear reason why they developed in this area but not at any other part of the central peak complex. The flows do, however, suggest some form of remobilization of material originating from the central peak, either by fluid injection or by some other process such as seismic shaking; in either case we would have expected to have seen a greater frequency of occurrence of the flows around the peak complex.

3.2. Pitted material

Pitted materials (Fig. 8) within impact craters on Mars were first recognized at Tooting crater (Mouginis-Mark et al., 2003). Our new mapping (Figs. 1b and 9) shows that pits can be found on the crater floor, in local topographic lows on terrace blacks (Fig. S8), and can occur out to radial distances of 4.3 km on the exterior rim of the crater. These pits commonly lack rims, are <50 m in diameter, and are usually sufficiently closely spaced that they share common walls (Fig. S9). However, in places where individual pits are found, they often possess a low rim. Topographic information from HiRISE

Fig. 8. Examples of pitted material on the southern part of the crater floor. See Fig. 3 for location. The largest pits in this oblique view are ~200 m in width. Note the raised rims on several of these pits. Segment of HiRISE image PSP_002158_2035.

DEMs reveals that the pits are usually <10 m deep (Fig. S10). The total surface area of pitted material, inside and outside the crater, is ~177 km^2.

To our knowledge, there are no lunar or Venus analogs to this pitted material, nor are the Martian pits similar to the hollows identified within craters on Mercury (Blewett et al., 2011). Tornabene et al. (2007), McEwen et al. (2007), Mouginis-Mark and Garbeil (2007), and Morris et al. (2010) have all suggested that Martian pitted materials are composed of either volatile-rich impact melt, or are impact-generated fine-grain sedimentary deposits. These authors also suggested that the pits are the result of undermining by collapse of voids caused by escape of volatiles or water/ice from this unit. Conversely, Hartmann et al. (2010) proposed a different origin, namely that the pits are due to sublimation. It is also possible that the pitted material is impact melt-rich breccia, but that the pits are formed by degassing of this suevite in a manner similar to that of the Ries crater fall-back suevite.

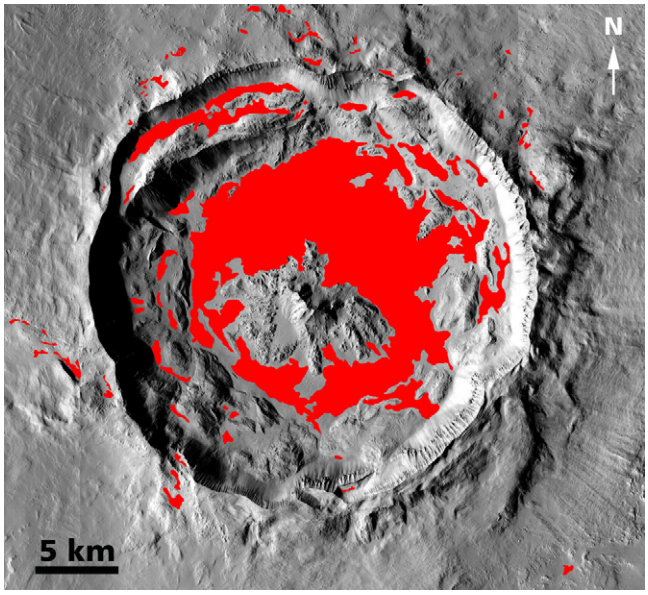

Fig. 9. Distribution of pitted material (shown in red) within Tooting crater. Note the few small outliners beyond the rim crest, most notably on the northern and SW rims. An extensive area of pitted material is also located on the large NW terrace block. Base image is CTX frame P01_001538_2035.

3.3. Fractured floor material

Mouginis-Mark and Garbeil (2007) identified a polygonally-fractured unit on the southern portion of the crater floor (Fig. S11). This fracturing is similar in morphology to the fractures observed within impact melt identified in lunar craters such as Tycho and Aristarchus (Strom and Fielder, 1971), Copernicus (Howard and Wilshire, 1975), and King (Heather and Dunkin, 2003). No fracturing can be identified on the northern floor, which appears to be more mantled. The difference in floor morphology coincides with the general depth characteristics of the crater, namely that the fractured unit is found at the lowest points of the crater floor (at an elevation of ~−5130 to −5050 m relative to Mars datum) while the northern floor is ~200 m higher than the southern floor. This elevation difference may be due to the collapse of the two large terrace blocks (Section 3.4) that re-distributed wall material onto the northern crater floor, burying the first-formed materials.

3.4. Blocks on crater floor

The relative lack of crater in-fill material allows numerous floor features to be identified that may be typical of features formed in many similar-sized Martian craters, but that have not been previously recognized because of the higher degree of degradation that has taken place elsewhere. We find examples of partially-buried wall blocks (some a few kilometers in size) that are now surrounded by the pitted material, and other blocks of probable sedimentary origin.

Three different attributes of the floor provide insights into the physical properties of the floor materials. First, the edges of two isolated blocks on the floor show ample evidence for sapping of the block (Figs. S12–S14). These blocks have relatively low relief (<250 m) and are physically removed from the wall units, implying that there is no source of volatiles except from within the unit itself. They are likely to be highly fractured by the cratering event and hence capable of easily releasing any trapped water that they may contain. Unlike other Martian craters where it has been proposed that late-stage rainfall associated with the volatiles took place during the cratering event (Williams and Malin, 2008), we find no evidence for an extensive catchment area, or for water carved channels, on the surfaces of these blocks. The material within which the sapping appears to have occurred has a smooth morphology but overlies bedded materials that may be remnants of a terrace block.

A second type of block on the southern floor has a crenulated surface with flow lobes that are ~30–45 m thick (Figs. S15 and S16). This block is at the base of the crater wall where possible impact melt is located. We interpret this floor block to be an example of remobilized impact melt that slumped down the inner wall from the southern rim early in the rebound stage of the evolution of the crater cavity because we can see evidence for sediment flows lying on top of this block (see Section 3.9).

Finally, we find few examples of fault blocks on the floor, but the clearest example is an apparent scissor-fault on western floor (Fig. S17). This tilted block of the rim material is now buried in the middle of the crater floor. The scarp of the block has a maximum height of ~200 m. Inspection of the surface of this fault block (Fig. S18) reveals layering and spur-and-gully erosion that is essentially identical to the morphology of the crater rim (see Section 3.8), suggesting that this is almost certainly a segment of the rim that slumped towards the center of the crater cavity.

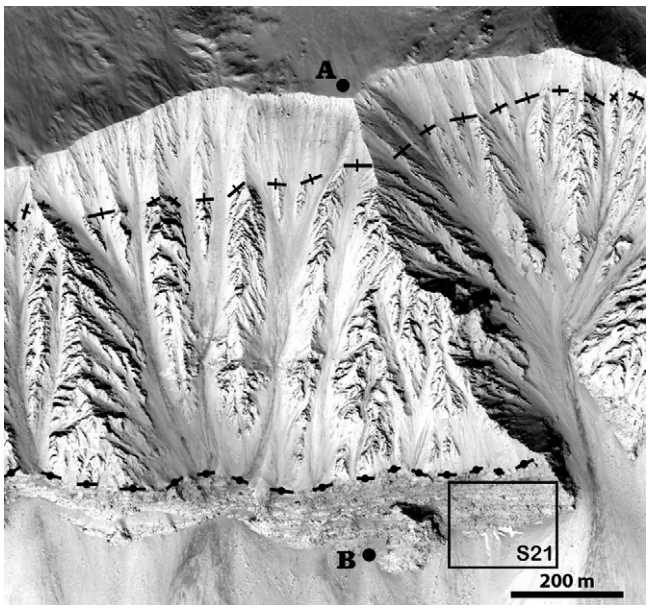

Fig. 10. Layering within eastern wall of Tooting crater. See Fig. S19 for location. Three distinct units can be identified in this vertical section, which is ~590 m high between points "A" and "B". The exterior ejecta deposits are at the top of the image and the rim crest is at "A". Directly below the rim crest is a layer of bland morphology. Between the dashed lines (dashed with cross-barbs at top, dashed with dots at bottom) is a more dissected layer that resembles badlands topography (Fig. S20). Below the lower dashed line is a sequence of layers, most likely the pre-impact lava flows that formed the target material. The lower part of the sequence of flows is covered by talus. The box at lower right marks the location of Fig. S21. Part of HiRISE image PSP_007907_2035.

3.5. Crater walls

The inner wall (Fig. S19) provides an outstanding opportunity to investigate the rim stratigraphy of a deep (~1850 m) impact crater on Mars. Three distinct layers can be identified within the top 600 m of the sequence (Fig. 10). Topmost of these layers is the rim crest, which has a bland morphology. Below this layer there is a more dissected unit (Fig. S20) which has a morphology reminiscent of badlands terrain on Earth. In the terrestrial case, "badlands" is a landscape where softer sedimentary rocks have been extensively eroded into steep slopes covered with loose dry soil. At Tooting crater, we interpret this middle unit to be extensively eroded unstratified primary ejecta that has been sufficiently "mixed" by the impact that it no longer preserves the target stratigraphy. Below this badlands unit is a sequence of almost horizontal layers that are morphologically similar to lava flows exposed in a graben at Arsia Mons volcano (Mouginis-Mark and Rowland, 2008), and we interpret the layers to be uplifted lava flows that were within the target material prior to the impact. The top of this sequence of lava flows is at an elevation of −3635 to −3614 m relative to the Mars datum, which is 237–258 m above the surrounding pre-impact surface, and thus defines the amount of structural uplift at the preserved rim. The rim crest is at an elevation of ~−3080 m, implying that structural uplift is ~30% of the total elevation of the rim crest, and that the thickness of ejecta lying upon the uplifted target rocks is ~550 m at this location. The lower part of this sequence of flows is covered by talus.

At the base of the exposed lava flows, and above the talus material, is a discontinuous outcrop of high albedo material (Fig. S21). Repeat imaging (between April 2008 and August 2010) of this material by HiRISE over more than one Mars year has shown that there is no change in the outline of this bright material so that it does not appear to be exposed ice, nor are the unit's color characteristics consistent with fresh ice within craters observed by HiRISE (Byrne et al., 2009). Thus this material may be more akin to "White Rock", which is an enigmatic crater interior deposit with a high albedo that may be an evaporite deposit (Williams and Zimbelman, 1994); in the case of Tooting crater, this high albedo material may have formed by the evaporation of salt-rich fluids leaking out of the crater wall. We have found no other outcrop of this high-albedo material anywhere within the crater cavity.

On the eastern side of the crater, the base of the badlands unit displays theater-headed canyons (Fig. S22) that, elsewhere on Mars, are typically attributed to water leaking from the substrate (Laity and Malin, 1985; Malin and Edgett, 2000). While the role of sapping is controversial in producing such canyons on Mars (Lamb et al.,

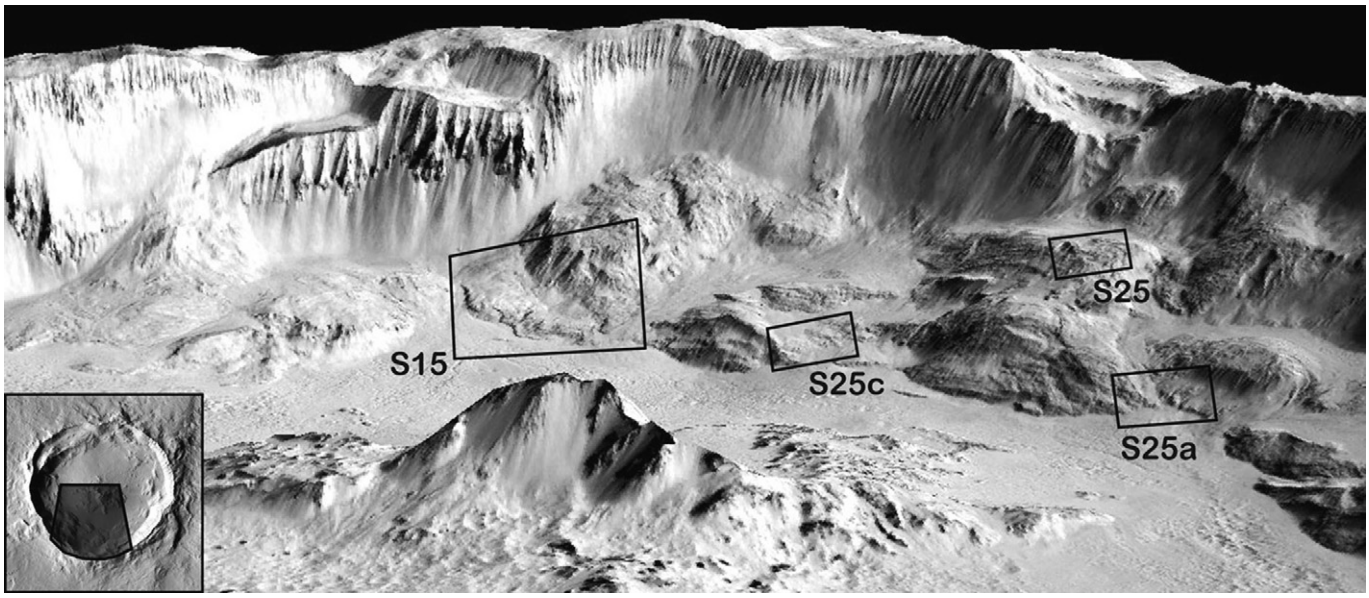

Fig. 11. Oblique view looking south at the interior of Tooting crater. The kilometer-high central peak is in the left foreground. Boxes delineate the locations of the HiRISE subscenes presented in Figs. S15 and S25. Base image is CTX frame P01_001538_2035, vertical exaggeration is 1.9×. The rim rises ~2100 m above the crater floor. Shaded area within insert at lower left shows the large image location within Tooting crater.

2006), the highly fragmented and fractured nature of the ejecta and crater wall materials make the occurrence of this process much more likely. We speculate that these canyons have been carved by the release of water trapped within the ejecta where it encountered the lava flows; aquicludes may permit water to reach the surface at these localities (Gilmore and Phillips, 2002). Although the temporal coverage of our image data sets is not as good as that for the craters investigated by McEwen et al. (2011), we have not found any evidence to suggest that this water release is occurring at the present time. The recurring slope lineae identified by McEwen et al. (2011) are located on the equator-facing slopes, whereas the features we have found (Fig. S23) are on the westward facing slopes. We also find similar evidence for massive, unconsolidated ejecta deposited on top of uplifted lava flows in the northwestern wall (Fig. S24). Headwall erosion of the rim has produced several large (>150 m diameter) pits within the topmost rim units (interpreted to be unconsolidated ejecta), which is ~150 m thick at this locality. The base of the unit lies above a series of layers equivalent to the lava flows shown in Fig. 10. These lava flows are ~260 m above the pre-impact target, almost identical to the elevation of the unit within eastern wall, and hence imply a similar amount of structural uplift.

On the southern inner wall (Fig. 11), there is additional morphologic evidence of water release from the target material after the crater formed. Some of the wall units are the source of debris that is superposed on the pitted terrain on the crater floor and hence post-dates its formation, whereas in other places the chronology is the opposite with canyons carved before pitted terrain formed (Fig. S25a and b). Slump blocks of wall material reveal episodes of water release, producing lobate flows that post-date the formation of some units of pitted material (Fig. S25c and d). At higher elevations above the crater floor, braided channels with a rudimentary dendritic pattern trend downslope and appear to be carved into a slumped block of wall material (Fig. S25e and f). In none of these cases, however, do we see evidence for any lobate debris aprons similar to those that have been attributed to episodic Amazonian glacial events (Morgan et al., 2009), suggesting that the volatile release involved a liquid (rather than ice) that was released soon after impact.

3.6. Sediment flows on the inner walls

Morris et al. (2010) identified a single large, lobate, flow on the inner wall (Fig. 12). The source region for this flow lies between two discrete wall terrace blocks and it is characterized by a centripetal network of channels that flow toward the crater floor. The flow is ~1800 m long and its width varies between ~250 and 500 m. The CTX DEM indicates that the probable source for the flow occurs at an elevation of ~4600 m and the distal end of the flow is at an elevation of ~4850 m, indicating the flow traverses a slope of ~8°. The source area is ~1500 m below the rim crest and ~400 m above the present-day crater floor (Figs. S19 and S26). The distal 600 m of the flow is composed of ~6 discrete lobes that are each ~10–15 m in width (Fig. S27) and stopped on a slope of ~9°. The distal lobes appear to be smooth with steep margins, prominent narrow levees (<3 m wide), and appear to have very few boulders on their surfaces. The distal lobes do not appear to coalesce; rather, they appear to have progressively overridden or have been deflected by previously emplaced distal lobes.

3.7. Terrace blocks

Tooting crater experienced two major collapse events within the cavity, forming large terrace blocks on the NW (Fig. 13) and NE inner walls of the cavity (Morris et al., 2010). Our geologic mapping of the floor material (Fig. 1b) reveals that these collapse

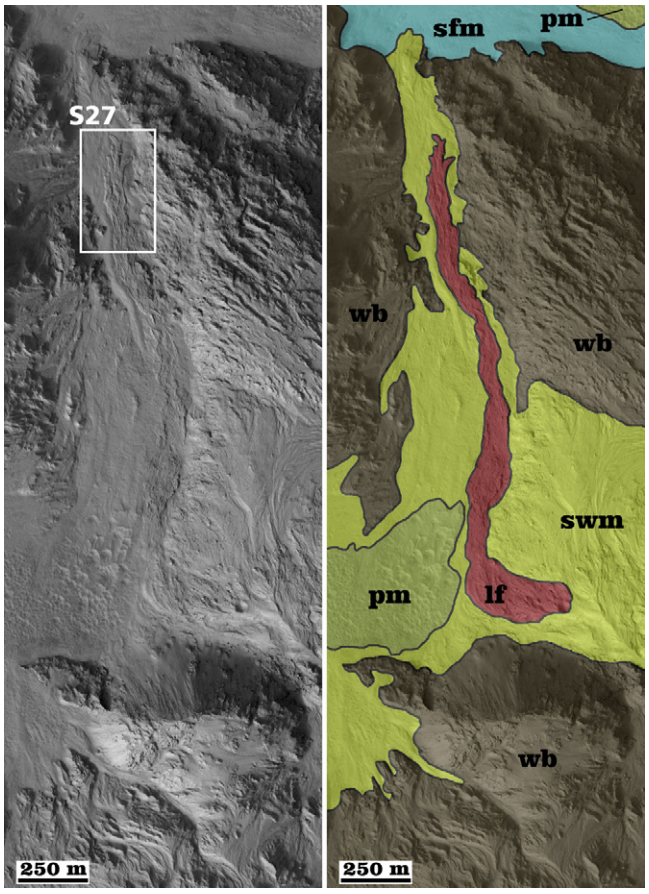

Fig. 12. Left: part of SW inner wall, showing location of a lobate flow. See Fig. 3 for location. Part of HiRISE image PSP_003569_2035. Box shows location of Fig. S27. Right: Interpretive geologic map, modified from Morris et al. (2010). "wb" wall blocks", "pm" pitted material, "swm" smooth wall material", "lf" lobate flow, and "sfm" smooth floor material.

events took place before much of the fill material was emplaced, as shown by the lack of deformation of the pitted materials (Section 3.2) and the embayment of segments of the eastern side of the crater. These terrace blocks have enlarged the crater radius by ~1.5 km, as measured radially away from the central peak. The non-slumped diameter is 25.7 km and the NE/SW diameter is 27.5 km, resulting in a "notch" in the perimeter of the eastern rim. There are also terrace blocks on the southern rim (Fig. S28), but these collapse events did not proceed to the same extent. The timing of all of these collapse, and near-collapse, events is discussed in Section 5.1.

3.8. Geomorphology of a heavily cratered area on the rim crest

Fig. 14 reveals a heavily cratered segment of the southern rim crest. Unlike most segments of the rim, numerous heavily degraded craters that are ~20–70 m in diameter can be identified (Fig. S29). These craters lack raised rims and have flat floors. Most revealing is that there are a few examples of craters that have lobate flows that originate from the surrounding rim deposits and partially infill the craters (Fig. S29). The interpretation is that the flows are impact melt, and thus the craters must have been formed very early in the cratering process. We propose that this surface may have been formed by fall-back that cratered the surface during crater excavation and that subsequently this surface failed to have impact melt emplaced upon it. Only the western and southern portions of the rim crest display this type of secondary impact cratering.

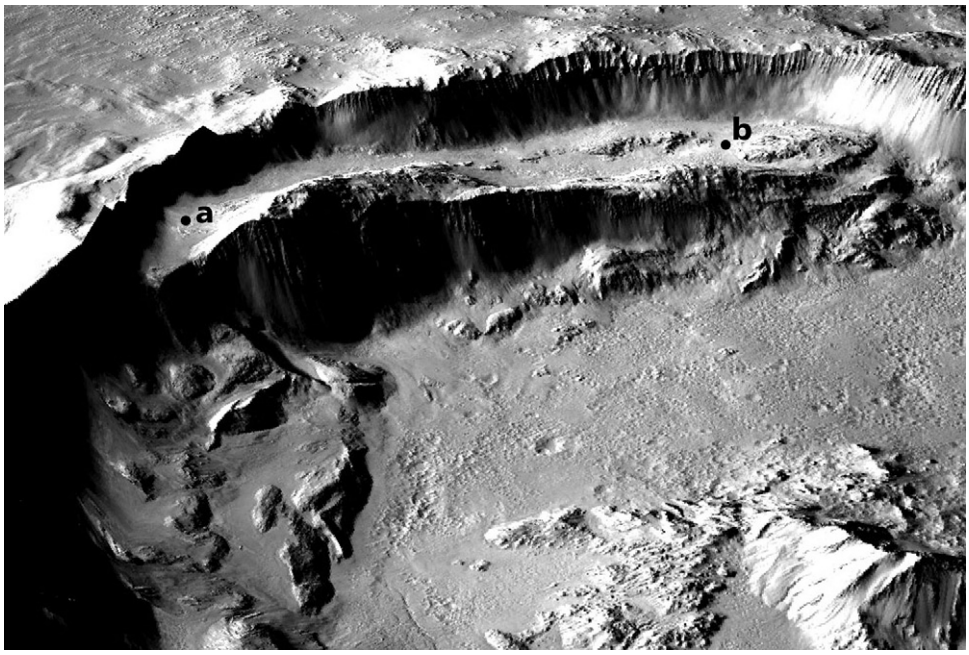

Fig. 13. Oblique view of large terrace block on NW wall. The flat part of terrace is ~865 m above the crater floor (see also the topographic profile across this terrace block shown in Fig. 5). Note that this terrace is tilted down towards the north (right in this image), with point "b" ~380 m lower than point "a". Base image is CTX frame P01_001538_2035. Vertical exaggeration is ~2×.

3.9. Impact melt

Morris et al. (2010) documented smooth materials with lobate flow fronts that extend up to ~2 km from the crater rim (Fig. 15). There appear to be several layers of this material which have been remobilized where the local gradient increases. Elevation measurements from an HiRISE-derived DEM indicate that the local slopes for these flows vary from 4° to 22°. The impact crater density superposed on this smooth material is identical to the crater density on ejecta in other locations on the crater rim, indicating that it is all the same age (Fig. 4). This material is morphologically similar to fresh impact melt deposits identified on the Moon (Strom and Fielder, 1971; Guest, 1973; Bray et al., 2010). Individual flows display smooth margins and lobate distal ends (Fig. 15). In some instances, on slopes of ~6–9°, the surface of the flows is characterized by folded "festoon" ridges (Figs. S30 and S31) in a similar manner to certain thick lava flows on Earth and Mars (Fink, 1980; Theilig and Greeley, 1986). Where the material is present on the edge of the rim, it exhibits some degree of coherence as there are obvious overhangs and a high degree of erosion beneath the overhang (Fig. S32). Fig. S33 shows a short (~100 m long) lobate flow comprised of this material that possessed high yield strength at the time of emplacement, as evidenced by the boulders on its surface and thickness. This flow is ~7 m thick at its distal end and stopped on a slope of ~5°.

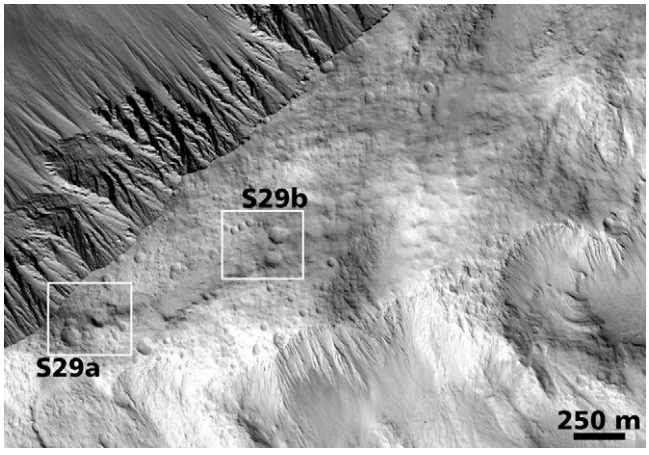

Fig. 14. This cratered segment of southern rim crest suggests that the crater rim was heavily cratered during the terminal phase of formation of Tooting crater. The absence of this unit elsewhere around the rim indicates that it has either been destroyed by subsequent rim collapse into the cavity, or that the rim was subsequently buried by late-stage flow of the ejecta. Boxes show locations of Fig. S29a and b. See Fig. 3 for location. Part of HiRISE image ESP_014157_2035.

3.10. Sediment flows on the outer walls

Four other types of flow, all located within 2 km of the rim crest, occur on the southern rim or on the southern interior wall of the crater ~1500 m below the rim crest (Morris et al., 2010). These flow features exhibit a range of flow morphologies, including transverse ridges, raised levees and boulders on their surface and margins. For example, in one 2.4 km by 2.7 km area on the southern rim between polygonally-fractured ejecta, there is a concentration of flows that appear to have originated as break-outs from within the hummocky ejecta on the exterior rim (Fig. 16). The largest of these flows is ~1260 m long and ~225 m wide, has an average slope of ~3°, has a hummocky morphology and appears to have originated directly from collapsed terrain (Figs. S34 and S35). This flow has a central channel that is ~490 m long and ~85 m across at its widest, and the channel floor has several isolated, elongated features (longitudinal bars) that are similar in morphology to the levees. The outer margin of the flow is characterized by individual lobes on a scale of tens of meters. The smooth, smaller, flows (Fig. S34) typically exhibit coalescing morphologies, with enclosed in-liners of the pre-existing surface ("kipukas") visible within some flows. Some of the smallest flows identified in this area by Morris et al. (2010) are of the order of tens of meters in length and only a few meters across.

Morris et al. (2010) also identified a lobate flow on the SW outer rim (Figs. S36 and S37). The source for this flow appears to be

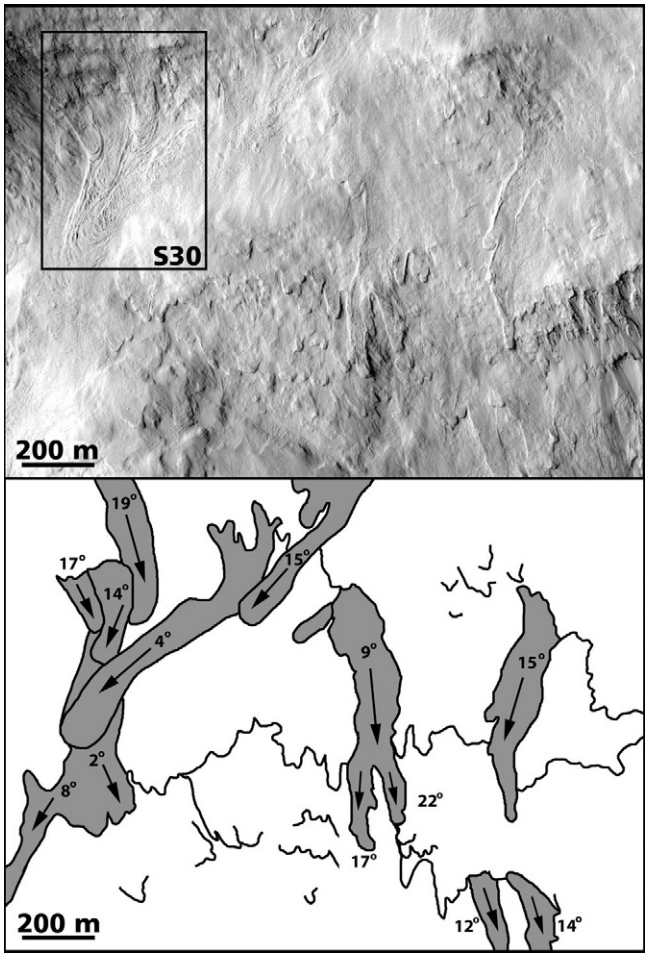

Fig. 15. (Top) Melt sheet on the southern rim. Downslope direction is towards the bottom of the image. Box indicates location of Fig. S30. Part of HiRISE image PSP_001538_2035. (Bottom) Interpretive map showing individual flows (shaded) and lobate margins of what are inferred to be smaller flows. Arrows indicate the interpreted flow direction, and average slope (in degrees) for each of these flow lobes is indicated. Note the multiple episodes of flow movement that are indicated by the superposition relationships of these lobes. See Fig. 3 for location.

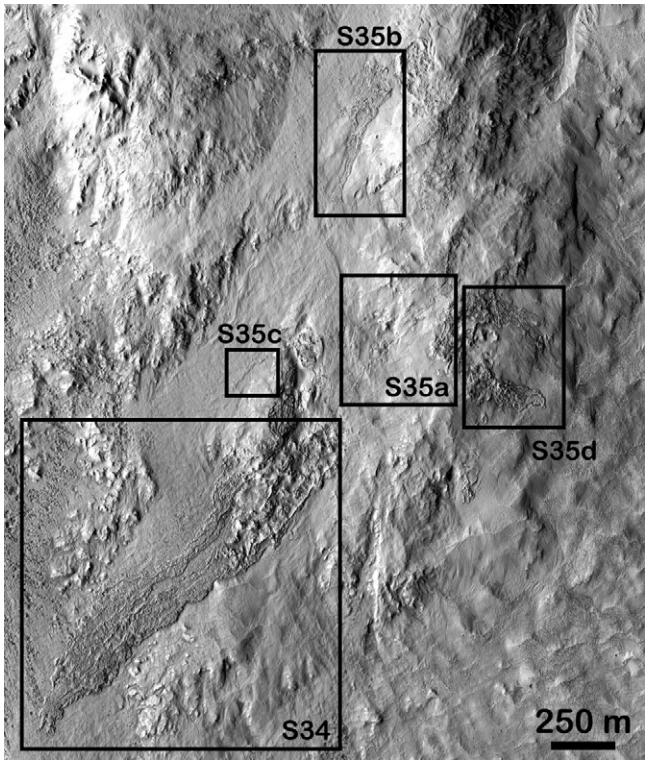

Fig. 16. Five examples of lobate flows on the southern rim that appear to have formed as break-outs from within the hummocky ejecta materials on the rim. Boxes outline the areas shown at higher resolution in Figs. S34 and S35. See Fig. 1a for location. Part of HiRISE frame ESP_016135_2030.

sediments collected on the rim between massifs of ejecta that were then remobilized by water originating from the ejecta. Topographic data indicate that the flow is <6 m thick along its entire length and that the margins are typically 2–4 m thick (Fig. S37). The flow increases in width down-slope from ~100 m near its source to a maximum of ~300 m, and has a channel with well-formed levees. At the distal end of the flow there is stratigraphic evidence indicating that there were pulses of material which produced multiple flow-fronts down-flow (Fig. S36a). The lobate margins with prominent levees in the channel suggest that surges occurred during flow formation, similar to the observed formation of large-scale experimental debris flows (Iverson, 1997; Major, 1997). Assuming that the source of the material in the flows was comparable to that in the adjacent parts of the ejecta blanket, the main control on the resulting flow morphology appears to be the relative amounts of volatiles and sediment, the particle size distribution of the sediment, and the underlying topography.

4. The ejecta blanket

4.1. Thickness variations

Because it formed on a virtually flat sequence of lava flows, Tooting crater provides a rare opportunity to investigate the geometry of the lobate ejecta layers that surround an impact crater on Mars. A total of 24,201 MOLA shots from 90 individual orbits lie on the ejecta blanket beyond the rim crest out to a radial distance of 64.0 km (Fig. S38). Mouginis-Mark and Garbeil (2007) used these individual MOLA elevation measurements to calculate the crater cavity volume (i.e., the volume of the cavity which lies below the −3872 m datum) as ~380 km^3, and the volume of materials above the elevation of the −3872 datum to be ~425 km^3. As described in Section 3.5, there is ~260 m of structural uplift of the inner wall but, because the radial decay of structural uplift from the rim is unknown, it is not possible to calculate the total volume of the ejecta or the net decrease in the mean bulk density of the ejecta compared with the pre-impact density of the lava flows.

Few previous studies have investigated the radial decay of ejecta thickness on Mars, but this most likely is related to the emplacement process (Garvin and Frawley, 1998; Garvin et al., 2003; Baloga et al., 2005; Barnouin-Jha et al., 2005; Mouginis-Mark and Baloga, 2006). The radial extent of the flow, the sinuosity of the distal margin, and the height of the distal rampart, may all be related to the degree of fluidization of the ejecta (Mouginis-Mark, 1978, 1979; Horner and Greeley, 1987; Barlow and Perez, 2003). Barlow (1994) has also proposed that the sinuosity of the rampart margins is an indicator of the volatile content of the ejecta at the time of its emplacement. Assuming a flat pre-impact surface and a base elevation for the surrounding terrain of −3872 m relative to the MOLA datum of Smith et al. (1999) allows the spatial distribution of the thickness of the ejecta blanket to be explored. Mouginis-Mark and Garbeil (2007) used point-by-point MOLA measurements of the thickness of the ejecta blanket (Fig. S39), and these interpretations can be improved with the use of a DEM derived from HiRISE stereo images. What is surprising is that the ejecta layers are remarkably thin; there are places where the distal layer is between 3 and 5 m

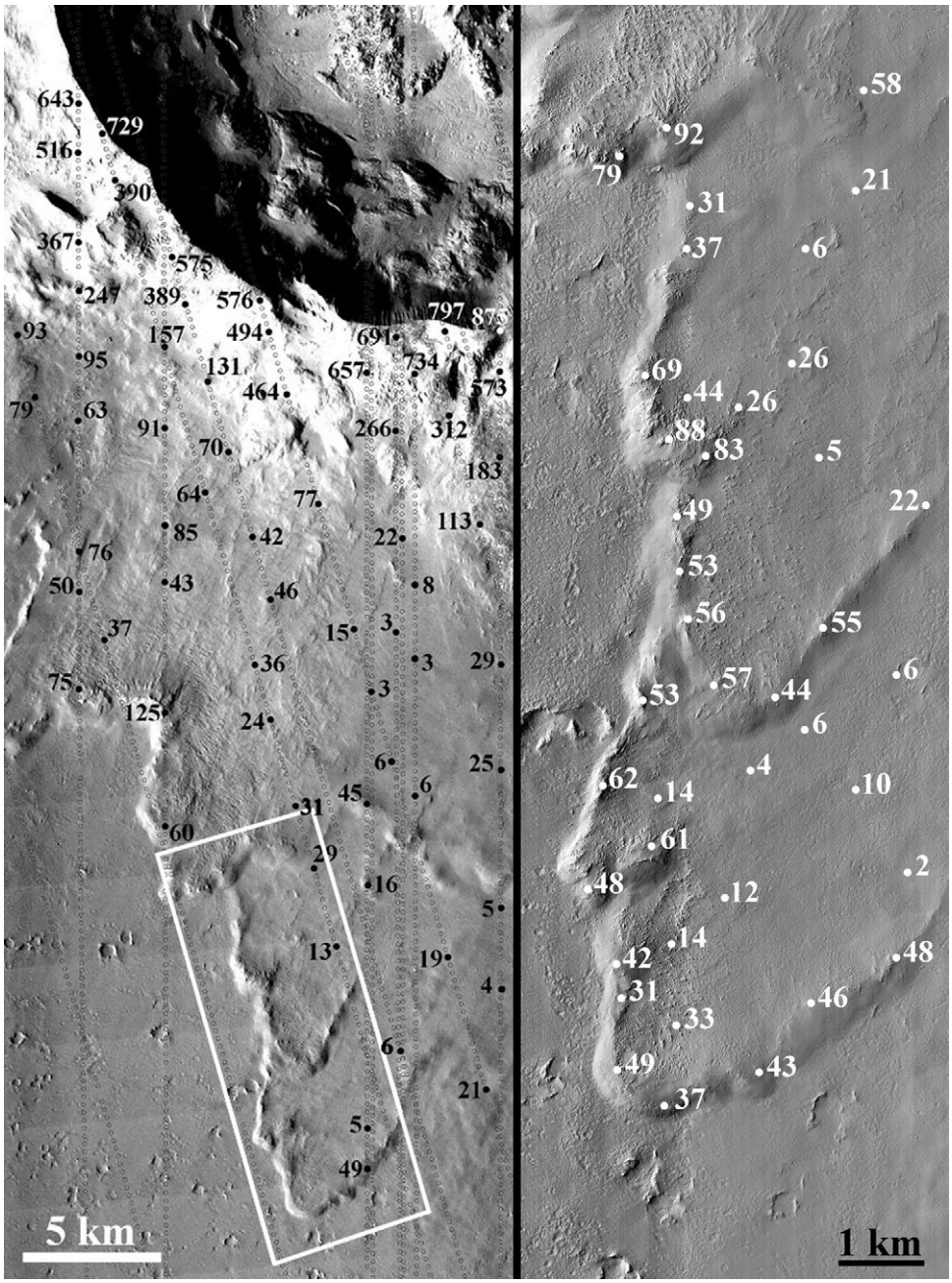

Fig. 17. Left: Spot thickness measurements of the ejecta layer south of Tooting crater. Values derived from MOLA data, and the height values (in meters) are elevation values relative to the −3872 m elevation referenced to the MOLA Mars datum. White box shows location of the HiRISE image presented at right. Faint lines of dark open circles mark the locations of individual MOLA shots. THEMIS VIS frame number V01990003. Right: Ejecta thickness values from HiRISE DEM, also relative to the −3872 m MOLA datum of Smith et al. (1999). HiRISE frame number PSP_007116_2035.

thick at radial distances of ~11 km from the rim crest, and just upslope from the distal rampart the layer may only be ~2 m thick (Fig. 17). The conclusion is that the majority of the distal ejecta lies in the ramparts, and that there is only a thin veneer in much of the outermost ejecta layer (see also Section 4.4).

4.2. Flow regimes within the ejecta blanket

Four different ejecta layers can be identified (Fig. 1b) within the ejecta blanket (Mouginis-Mark, submitted for publication), which implies a multi-phased emplacement process. These layers are well defined, with a scarp marking the boundary between each layer. The thickest layers are closest to the rim (Fig. 17). In addition to these four main ejecta layers, variations in surface texture can be observed within the layers (Fig. 18), with up to four different facies within a single ejecta layer (Fig. 19). The near radial symmetry of the four layers suggests individual pulses of material sweeping out in all directions from the rim crest of Tooting. The *smooth facies* is interpreted to indicate uniform flow with no relative velocity gradient within the layer. The *hummocky facies* is interpreted to characterize areas where ejecta flow over-rode pre-existing topography, most likely created by earlier components of the ejecta given the bland morphology of the surrounding target material. The *radial facies* is found down-range of discrete topographic obstacles such as large, partially buried secondary craters. The *crenulated facies* is predominately found close to the perimeter of the flow where the ejecta

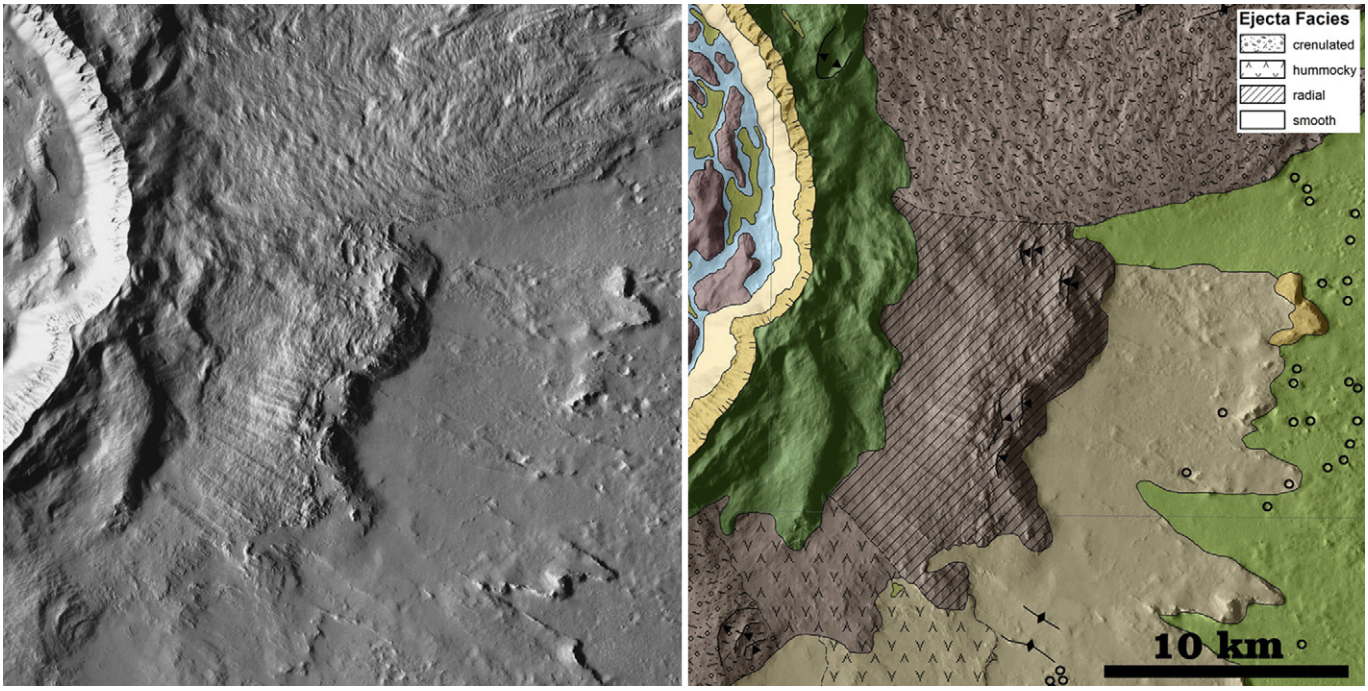

Fig. 18. Example of the diverse morphologies of ejecta layers to the east of the crater rim. At left is a THEMIS VIS mosaic. At right is geologic interpretation of the different ejecta layers (el2 [light green], el3 [light brown], and el4 [dark brown]) and the four different ejecta facies (Mouginis-Mark, submitted for publication). At left is eroded rim material, and the open circles denote buried secondary impact craters. See Fig. 1a for location.

layer had continued to flow after the distal rampart had formed, causing a general disruption to the layer surface.

Mapping of the layers and facies within the ejecta blanket does not reveal a mechanism of proximal transformation from ejecta excavation to overland flow close to the rim, but conceivably this process might have involved the collapse of steeply ejected volatile-rich target material or ballistic ejection of fluidized slugs (e.g., Gault and Greeley, 1978; Melosh, 1989). There are nevertheless morphologic similarities between the radial facies and the striations seen on certain terrestrial landslides (Shreve, 1966, 1968; McSwaveney, 1978). Once a ground-hugging flow is established, it is considered to have a well-defined thickness that may vary with distance and time. It is possible that there could be many types of particulate and fluid exchanges between the flow and the preexisting subsurface (Barnouin-Jha et al., 2005), and/or interactions with the ambient atmosphere similar to those discussed in connection with vortex-ring propagation (Barnouin-Jha and Schultz, 1996, 1998). Regardless of the details of the process, the morphologic evidence suggests that viscous flow often appears to start from close to the crater rim, but can also occur at greater radial distances where some form of inner ejecta layer is present.

An unusual block of material 1.3×2.4 km in size can also be seen on the western rim of the crater (Fig. S40). The scarp face of this block is ~250 m high and layering in the crest of the block is very similar to that observed on the crater rim crest. This block is enigmatic because it is the only example around the perimeter where a large segment of the rim crest was physically separated from the rim. No structural features (faults, graben, etc.) appear to be associated with the block, so that it is probably not an uplifted block. Similarly, no slide marks, deformation features, or landforms indicative of material flow around the block can be seen, so that our preferred interpretation is that the block was emplaced early in the formation of the ejecta blanket and is simply a coherent piece of the cavity that was ejected beyond the rim crest. No late-stage ejecta can be found at the crest of the block, and there is no evidence for radial erosion of the block crest by the passage of the ejecta layers.

4.3. Dewatering of the ejecta blanket

Numerous landforms observed within the ejecta layers point toward the layers being wet after their emplacement. These layers have variously been postulated to have been fluidized by target volatiles (e.g., Carr et al., 1977; Mouginis-Mark, 1987) or the atmosphere (e.g., Schultz and Gault, 1979). The clearest example of dewatering can be found on the eastern rim (Fig. 20), where a tilted block of ejecta $\sim 2.5 \times 8.0$ km in size faces back towards the crater rim. A network of valleys, with the dominant direction of flow towards the west, can be identified. In detail, these valleys may be steep-sided and display at least two episodes of formation (Fig. S41). Channels carved within the surface of the layers (Fig. S42) also hint at dewatering of the ejecta after it came to rest. Additional evidence for the ejecta containing water after it came to rest includes sediment fans (Fig. S43), which are inferred to have formed from the surface flow of water at the edges of distal ramparts.

4.4. Geometry and morphology of distal ramparts

Since the earliest days of data analysis during the Viking Orbiter missions (Carr et al., 1977) the distal rampart at the margins of the fluidized ejecta layers have been inferred to have formed as a result of flow of the ejecta across the surface. The origin of ejecta ramparts is controversial (e.g., Schultz, 1992; Baratoux et al., 2002; Baloga et al., 2005; Boyce et al., 2010). However, it is clear that these are primary flow features that resemble ramparts at the termini of geophysical mass movements such as landslides and debris flows and those found in some laboratory granular flow experiments, as well as in numerical modeling. Consequently, terrestrial landslides may offer a valuable analog to the ramparts. There is considerable evidence (Savage and Hutter, 1989; Iverson, 1997; Pouliquen and Vallance, 1999; Denlinger and Iverson, 2001) that the formation of marginal ramparts is the result of flow instability that grows from a high-friction band of coarse particles that naturally accumulates at the propagating flow margins of landslides and debris flows

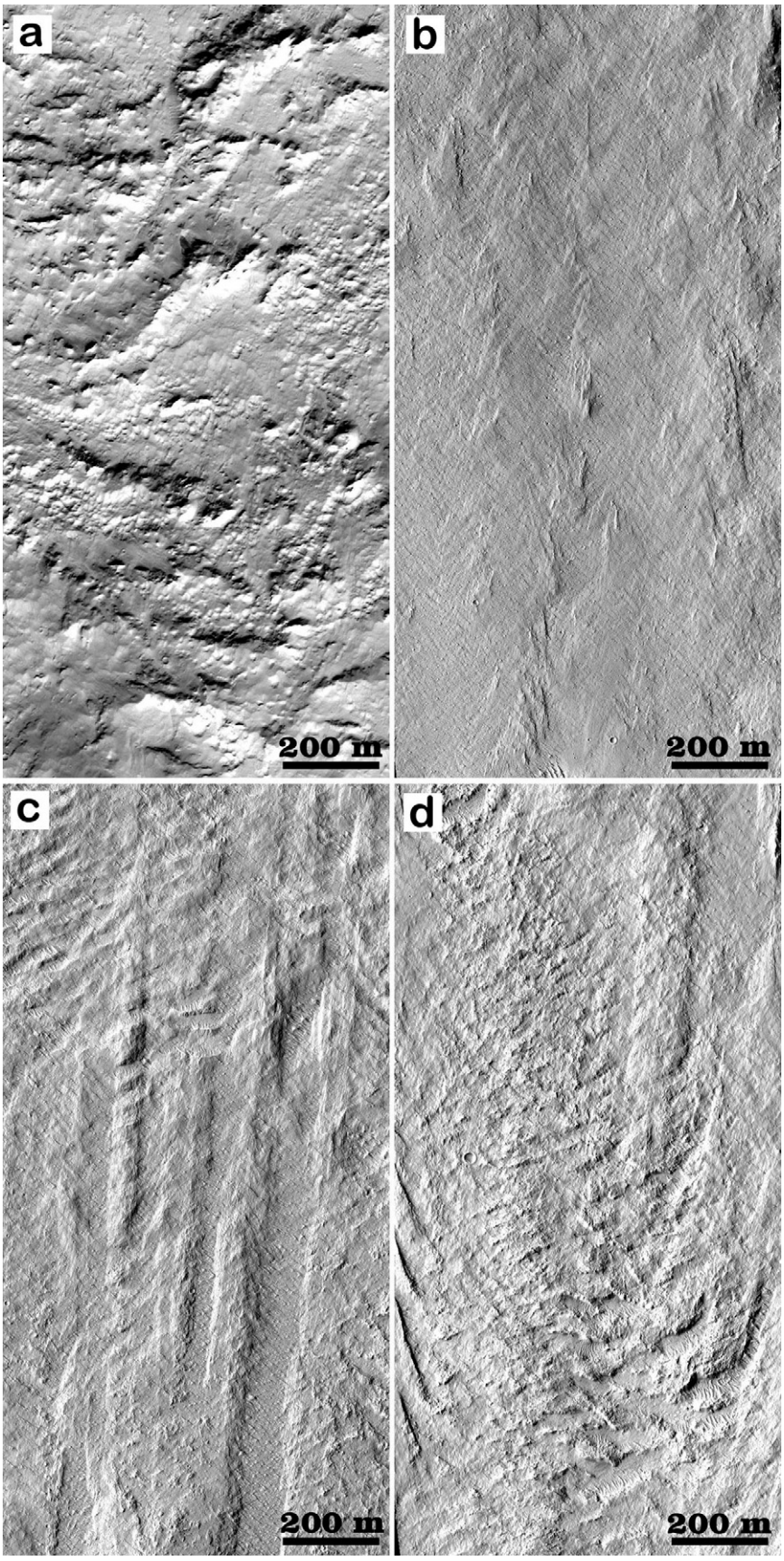

Fig. 19. Comparison of flow morphology for four different segments of the ejecta layers, showing the remarkable diversity in flow properties. All images have been rotated so that the flow direction is towards the top. (a) *Crenulated facies* where the ejecta piled up against an obstacle. (b) *Smooth facies* where, presumably, the flow was laminar. (c) *Radial facies* where streamers extend away from a buried secondary crater. (d) *Hummocky facies* that may form as ejecta moved over undulating basal topography. Top left frame HiRISE image PSP_007116_2035, other three images are from HiRISE frame ESP_017625_2040. See Fig. 1a for locations.

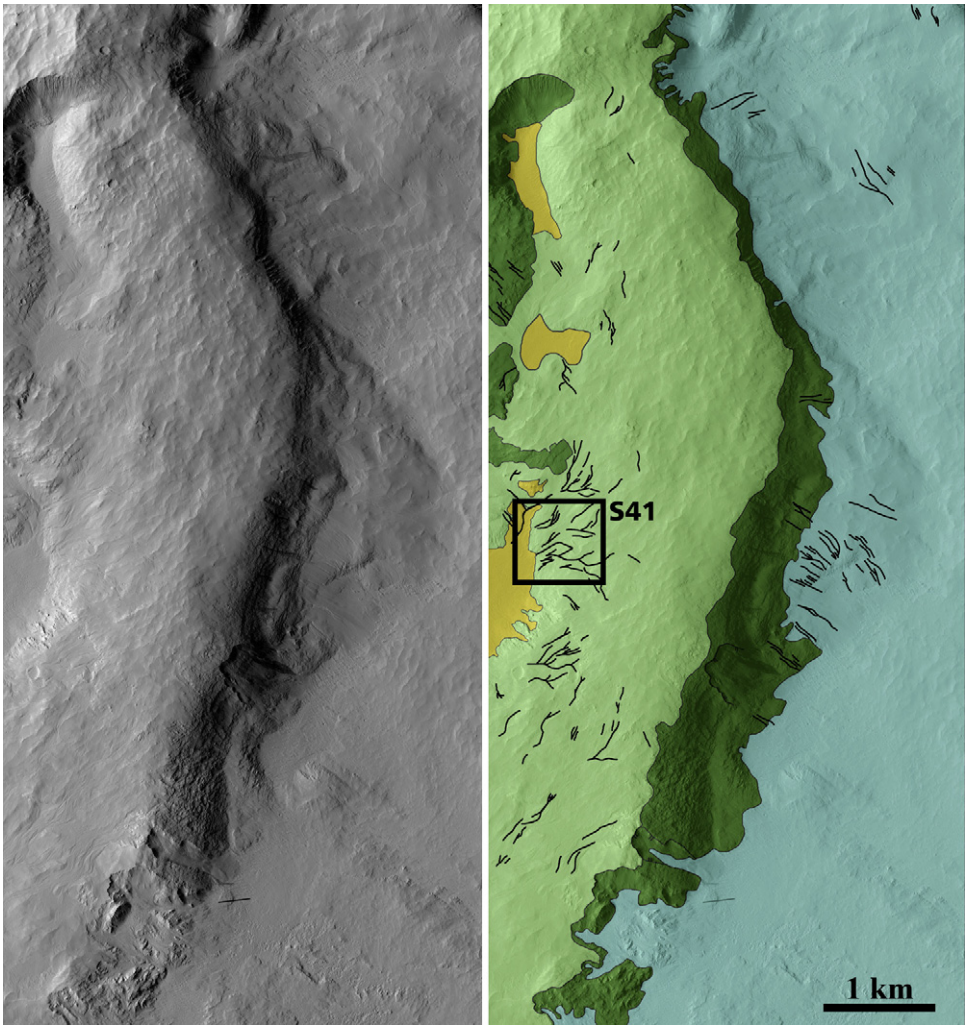

Fig. 20. On the SE exterior wall, a large segment of the exterior rim material displays numerous valley networks that suggest dewatering of the ejecta, with water flow towards the left of this image. The scarp (denoted as the dark green unit) is ~100 m high at the top of image and ~200 m high at bottom of image. At left is the HiRISE image, at right is a geologic sketch of the main units identified in this area. Box indicates the area shown in detail in Fig. S41. See Fig. 1a for location. Part of PSP_007907_2035.

(i.e., gravity-driven, thin flows of poorly sorted, wet, or dry cohesionless fragmented debris). Because the largest particles in natural grain flows are commonly more angular, as well as more massive, the coarse mixture of grains at the front of the flow has greater Coulomb friction than the finer grain debris that follows behind. As a result, this band of coarse particles tends to slow the flow and is pushed forward and up into a ridge from behind by the moving body of finer particles. The thermal inertia observation of Baratoux et al. (2005), and high block density reported by Barnouin-Jha et al. (2005) and Boyce et al. (2010) associated with Martian crater ramparts support this model.

By virtue of the preservation of the ejecta blanket, details of the topography and morphology of the distal rampart can be identified (Figs. 21, S44 and S45). The HiRISE-derived DEM indicates that the distal ramparts can be ~60 m high (Fig. S44), comparable to the heights of ramparts measured at other multi-layered ejecta craters (Mouginis-Mark and Baloga, 2006). Rampart widths, as measured in the radial direction away from the parent crater, are more difficult to measure accurately because a large degree of subjectivity enters into the determination of the rampart extent in the image data (Baloga et al., 2005). The outer slope of the rampart is quite steep (~25°), so it is relatively easy to identify the distal extent. However, the inner slope is much shallower (~5°), so it is much harder to ascertain the location at which the deposit begins to ramp up to form the rampart, due to the illumination geometries of the surfaces under study. From the mapping of Mouginis-Mark (submitted for publication), the total surface area of the ramparts is 1147 km^2. We note that there are numerous "radial ramparts" within the ejecta layers, particularly in the NW segment of the ejecta blanket (Figs. 21 and S45). These radial ramparts have not been discussed in the literature before, but their dimensions and locations likely provide useful information on the manner in which the ejecta flows deposited material as they decelerated.

Baratoux et al. (2005) identified a systematic temperature increase at night at the edge of the ramparts that is most likely related to a particle size distribution inherited during the emplacement of the ejecta layers. A kinetic sieving process akin to that observed in naturally-occurring flows such as volcanic pyroclastic flows was proposed as responsible for the temperature increase (Baratoux et al., 2005). They also suggested that the ejecta morphologies having a less sinuous outline may have experienced a more efficient sorting of particles and this implies a lower volatile concentration. However, due to the pervasive coating of dust, it is not possible to collect good thermal inertia data for Tooting crater. Qualitatively, nighttime THEMIS IR data show that the distal ramparts are relatively warm, but no estimate can be derived for the block distribution within the ramparts compared to the rest of the ejecta layers.

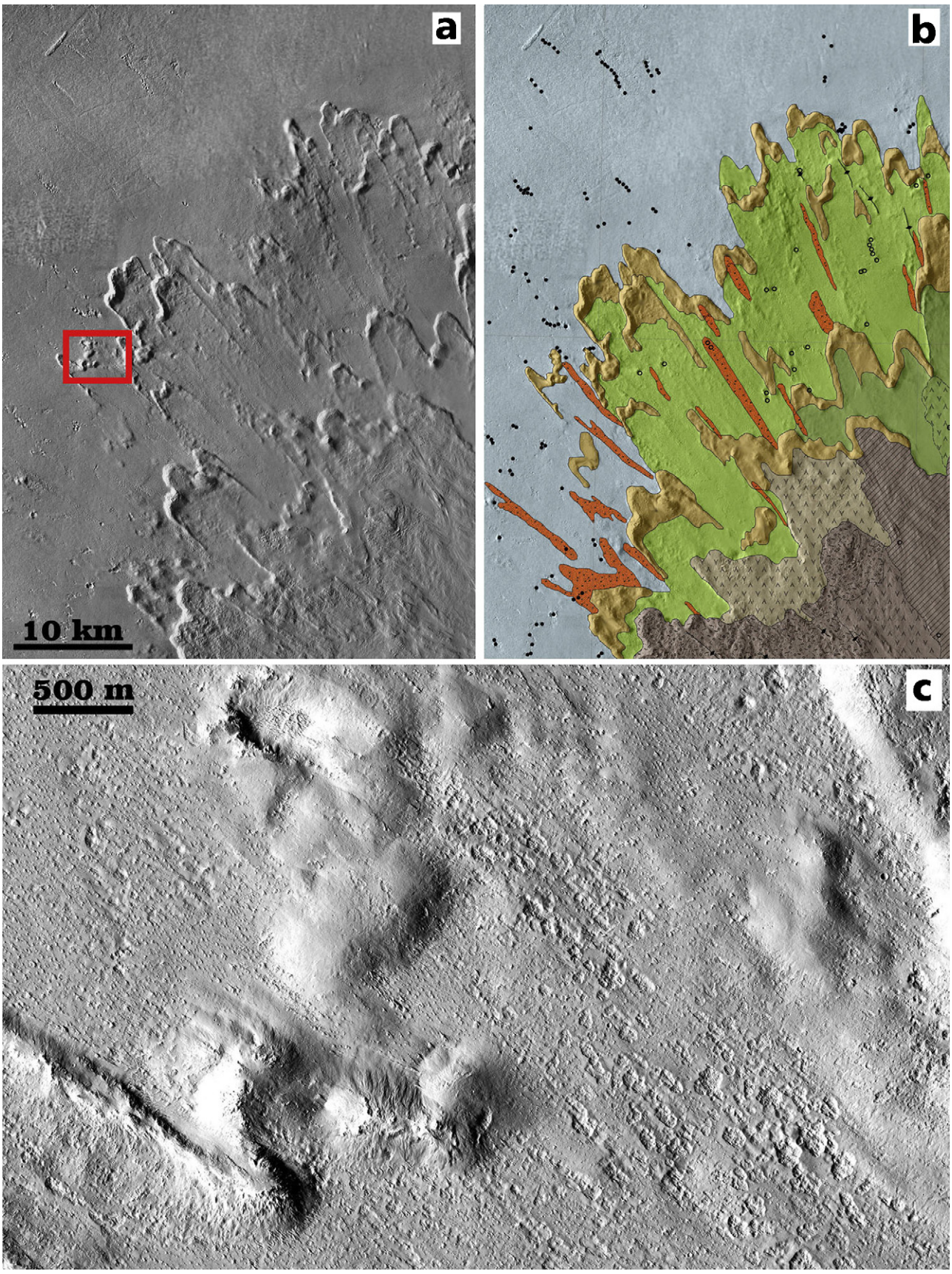

Fig. 21. Ejecta layers NW of crater. (a) THEMIS VIS mosaic, red box indicates coverage of image at bottom. (b) Part of the geologic map of Mouginis-Mark (submitted for publication), showing same area as in "a". (c) Details showing the streamers of "crater clusters" that do not appear to be secondary craters, but that cross the ejecta layers and the distal ramparts. Their mode of origin is unknown. Part of HiRISE image ESP_016346_2040.

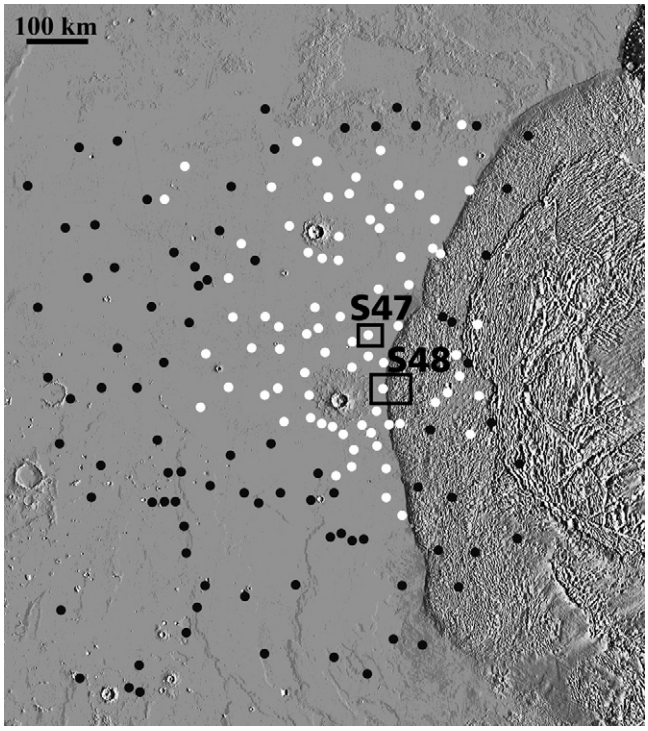

Fig. 22. Distribution of secondary craters from Tooting crater, as identified from 18 m/pixel THEMIS VIS images. White dots denote areas where secondary crater chains have been identified, and black dots denote THEMIS VIS images that show that secondary craters are not present. Note the strong asymmetry in secondary crater distribution, with the majority of ejecta distributed to the NE of the crater. White rectangles denote areas shown in Figs. S47 and S48. Base map is a shaded relief image of the area, derived from MOLA 128th-degree DEM with illumination simulated from the right.

The ramparts display a morphology that is probably associated with a process that operated once the ejecta came to rest. Many pits occur at crests of distal ramparts (Fig. S46). These pits are <30 m diameter, are approximately circular in plan-form, and occur in closely-packed clusters often containing a dozen or more pits and appear to be collapse features. We interpret these pits to have formed by collapse since they lack rims or secondary ejecta, thereby discounting the idea that they are either secondary craters or explosion craters.

4.5. Secondary crater distribution and morphology

By virtue of the young age of the impact (~2.9 Ma; Fig. 4), secondary craters from Tooting crater are easy to identify (Fig. 22). We have used all the THEMIS VIS images available through December 2010 to map the distribution of secondary craters. We identify distal secondary craters using the same criteria developed for the Moon (Guest and Murray, 1971; Oberbeck and Morrison, 1973) and other Martian craters (Tornabene et al., 2006; Calef et al., 2009). In addition, 315 subdued pits >200 m in diameter have been mapped (Mouginis-Mark, submitted for publication) within the ejecta layers, and are interpreted to be buried secondary craters (Fig. 23). These buried secondary craters occur as close as 8.3 km to the rim crest, and typically are found within the outermost two ejecta layers.

Because of the large number of secondary craters observed in some localities, we have used the presence/absence of secondary craters within individual THEMIS VIS frames to map out the general distribution of the ejecta (Fig. 22). A typical set of secondary craters in the diameter range ~100–300 m is illustrated in Fig. S47, which is located ~110 km from the rim crest. The maximum range

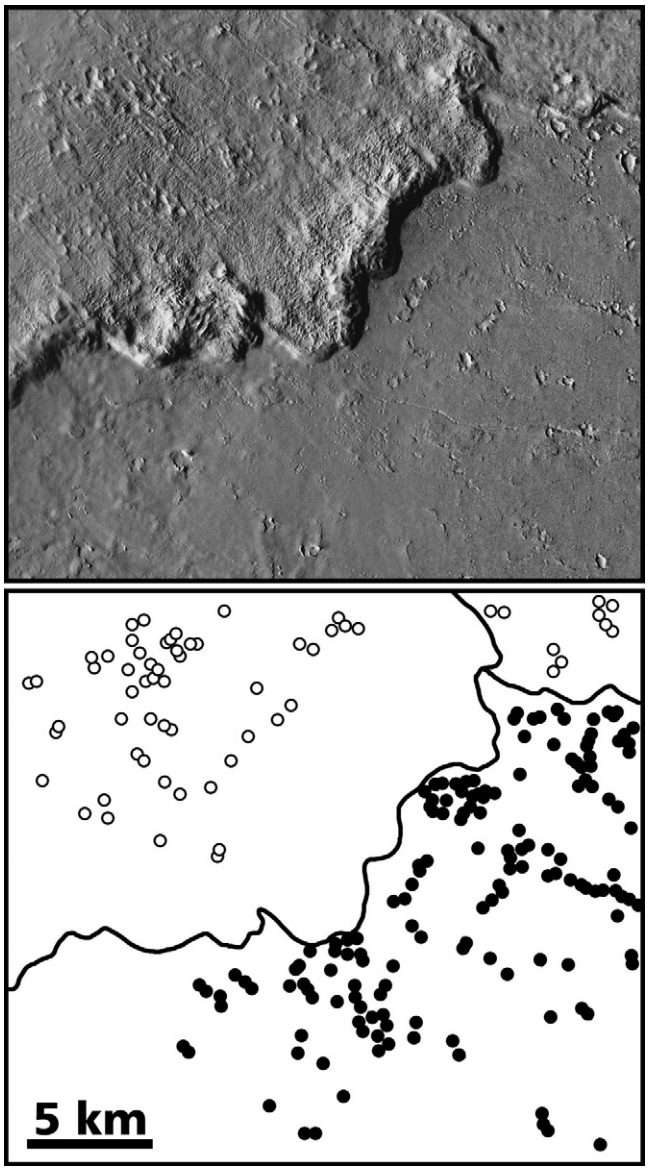

Fig. 23. Top: Example of secondary craters over-run by lobate ejecta layers. Direction of flow is towards lower right of image. See Fig. 1a for location. Bottom: Interpretive sketch of image at top. Open dots indicate secondary craters that are partially buried, and closed dots indicate unburied secondary craters. Black lines denote boundaries of ejecta layers. THEMIS image V05710012.

of identifiable secondary craters is ~500 km (~36.0 radii from the rim crest) in a NE direction and ~465 km (34.1 radii) in a NW direction. In contrast, secondary craters are only identifiable ~215 km (15.8 radii) to the SE and 225 km (16.5 radii) to the W. Significantly, in view of the possible oblique impact from the SW proposed by Morris et al. (2010), secondary craters can only be found out to a radial distance of ~40 km from the rim crest in a SW direction. Such radial distances are appreciably less than the 1600 km identified by McEwen et al. (2005) and Preblich et al. (2007) for the distal secondary impact craters from Zunil crater. Unlike the Zunil secondary craters that are concentrated at distances beyond ~16 crater radii (~80 km) from the crater rim, the secondary craters at Tooting crater are found at the distal margins of the lobate ejecta flows, and we find good morphologic evidence that demonstrates that many secondary craters were formed much closer to the parent crater and were subsequently partially buried by the ejecta layers (Fig. 23).

We find streamers of secondary craters that radiate away from the crater on the western margin of the Olympus Mons aureole material (Fig. S48). The aureole materials are of unknown origin but may possibly have been formed by thrust faults (Borgia et al., 1990) or by giant landslides (McGovern et al., 2004). In either case, this part of the aureole materials was formed before the Tooting impact and show no signs of remobilization after crater formation.

Many pits, called "crater clusters" (Mouginis-Mark, submitted for publication), occur beyond the distal ramparts of the ejecta layers. These pits (Fig. S49) take the form of closely-packed streamers of depressions aligned radial to the parent crater and lack prominent rims. In some instances, these chains of craters extend up onto the ejecta layers and climb over the distal rampart (Fig. 21c), suggesting that they post-date the deposition of the fluidized ejecta. How these crater clusters formed is very problematic, because they seem to be a late-stage phenomenon that occurs only on the northern half of the ejecta blanket within ~10 km of the maximum range of the ejecta layers. Most troubling is the fact that the individual features within the crater clusters have a similar morphology on both the ejecta layers and the pre-existing terrain beyond the distal ramparts, thereby creating confusion in the interpretation of when (and how) these craters clusters formed.

4.6. Evidence for an oblique impact from asymmetric ejecta pattern

Two lines of evidence support the idea (Morris et al., 2010) that Tooting crater formed from an oblique impact. First, the distribution of the ejecta near the rim is asymmetric, with the least volume emplaced upon the SW rim and the greatest volume on the NE rim (Fig. S39). Secondly, the distribution of secondary craters (Fig. 22) illustrates that the greatest ejecta range (~500 km) is to the NE, with the least number of secondary craters observed to the SW. The asymmetry of ejecta with the least material in the (presumed) up-range direction can also be seen from the distribution of the fluidized ejecta layers, with the distal ramparts being closest (24.3 km) to the crater rim in the SW direction (Fig. 1a), while the ramparts are as far as 64.0 km from the NE rim.

5. Broader implications

Because Tooting crater preserves many of the features that are inferred to originate at the time of crater formation, it is possible to use the observations described here to place the crater in the broader context of impact craters on Mars, as well as investigate the cratering process. This section explores some of these implications.

5.1. Inferences about sequence of events for crater formation

We see evidence for the following chronology in the formation of the crater and the ejecta materials:

Stage 1: Following the initial formation of the crater cavity, the central peak and fractured floor material on the southern part of the crater floor appear to be the oldest preserved landforms. We do not find any evidence that supports vertical movement of the peak material following emplacement of the fractured floor material or pitted material (Fig. 7); for example, there are no small-scale structural features (i.e., fractures or compressional ridges) around the peak that would indicate vertical movement after the overlying pitted material formed.

Stage 2: The heavily cratered segments of the southern rim (Fig. 14) appear to be the oldest preserved segments of the rim crest, and probably represent the effects of fall-back ejecta at an early stage of cavity formation. Where large terrace blocks formed, such as the "rim" of the large terrace block on the NW side of the crater (Fig. 13), the heavily cratered units are absent and suggest that the process of terrace formation destroyed the heavily cratered material. This destruction appears reasonable, given that the topmost few hundred meters of rim topography appear to be unconsolidated ejecta (Fig. 10). The time of formation of the heavily cratered rim relative to the formation of the fractured floor material is unclear and could have been contemporaneous. We also note that we see no heavily cratered terrain at greater radial distances than the southern rim; the most likely explanation seems to be that erosion of the surface by the radial flow of ejecta has removed the craters.

Stage 3: Large-scale terrace formation took place after the formation of the heavily cratered segments of the rim, but before the formation of pitted material. However, because the pitted material shows evidence that it was initially a fluid (albeit a fairly viscous fluid) this pitted material could have been deposited on the terrace blocks before their formation and subsequently rode the terrace blocks down to their present location.

Stage 4: Outcrops of pitted material, as they currently appear, may have formed over a relatively long period of time (minutes to hours) after terrace collapse took place. We see no indicators of deformation within the pitted material on the northern floor at the foot of the large NW and NE terrace blocks, but see evidence that this material flowed onto the floor from the terrace blocks (Fig. S8). Pitted material appears to be a key stratigraphic horizon for the identification of the chronology of the crater evolution, as this material is widespread (Fig. 9), and overlies the central peak materials, terrace benches, and the near-field ejecta deposits. Many of the lobate flows believed to be produced by cavity dewatering (Figs. 12 and S25) over-lie pitted material. However, the stratigraphic relationship between pitted material and the slumped block of impact melt (Fig. S16) is enigmatic, with the impact melt potentially over-riding some of the pits.

Stage 5: Impact melt was emplaced after the fall-back ejecta on the southern rim. We find no evidence for the smooth sheet of the material interpreted to be impact melt (Fig. 15) being hit by high-angle trajectory secondary blocks ejected from the parent crater. Furthermore, probable impact melt flows can be found that partially in-fill the fall-back craters (Fig. S29).

Stage 6: Terrace formation on the southern rim took place before the impact melt solidified. The impact melt was still fluid after terrace formation because the melt was able to flow over the current topography and onto the slumped terrace block (Fig. S28).

Stage 7: The fluidized ejecta layers were relatively slow-moving, arriving at radial distances where secondary craters had already formed, either partially (Fig. 23) or fully burying these craters (Fig. 1b). However, we cannot definitively identify the chronology of the different ejecta layers and cannot say, for example, if the inner layer was emplaced before or after the outermost layer. Despite their young age, the morphology of the edges of the ejecta layers is already too degraded to determine the stratigraphy.

Stage 8: Dewatering of the cavity walls took place at a relatively late stage of the cavity's evolution and took place in multiple events, with flow units produced as discrete lobes originating from the middle elevations on the inner wall (Figs. 12 and S27).

Stage 9: Sapping took place late in the evolution of the crater cavity, and took place from units just above the layers interpreted to be uplifted lava flows within the target material (Figs. S22 and S23) and local topographic highs on the crater floor (Fig. S13). However, it is not clear if this sapping is currently taking place (as has been postulated for other craters; McEwen et al., 2011), although the low optical albedo of the flows (due to the lack of dust cover) strongly suggests an age much less than the age of the parent crater.

An important aspect of this sequence of events is the recognition that most of the key observations are made on the southern side of the crater. Only here do we see possible impact melt and surfaces cratered by fall-back, as well as the numerous flows on the inner and outer walls. One possible explanation for this distribution of landforms was proposed by Morris et al. (2010), who noted that slumping of the wall to produce terrace blocks around much of the perimeter of the rim except on the southern segment. Thus the greater degree of preservation of the earliest landforms at this location could be due to the lack of mega-slumping of the rim. Smaller terrace blocks are found on the southern rim (Fig. S28), and we speculate that the rugged terrain on the southern floor (Fig. S16) could be a slumped block with a veneer of impact melt. Large terrace blocks, such as the one on the NW side of the crater (Fig. 13), are absent in the southern part of the crater. Morris et al. (2010) further speculated that the southern rim did not collapse because of a smaller volume of ejecta emplaced in this area (Fig. S39), and that the southern wall was able to structurally support these ejecta without slumping.

5.2. Tooting crater as a possible source of some SNC meteorites

Several photogeologic (Mouginis-Mark et al., 1992; Tornabene et al., 2006) and spectral (Hamilton et al., 2003; Lang et al., 2009) studies have attempted to identify candidate impact craters or source areas for the SNC meteorites. Tooting crater was not included in any of these earlier investigations because of inadequate image coverage from the Viking Orbiter missions, and the presence of ubiquitous dust that precludes any compositional analysis. However, first the availability of THEMIS VIS images (Mouginis-Mark et al., 2003), and then subsequent higher resolution images (Mouginis-Mark and Garbeil, 2007; Morris et al., 2010), raises the possibility that Tooting crater could be the source of at least some of the SNCs.

There are two main clusters of ejection ages for SNC meteorites, containing 4 or 5 meteorites, that might be consistent with the age of Tooting crater. Clusters of meteorite ages occur at 1.16 ± 0.6 Ma and 2.9 ± 0.3 Ma (see McSween, 2008 for a summary of the petrology of the Martian meteorites). All of these rocks are igneous in origin, and are either basalts or ultramafic rocks. All of the rocks were probably located on or very near the surface at the time of their ejection towards Earth because numerical models indicate that spallation of surface or near-surface materials around craters are the only target rocks accelerated to Martian escape velocity (Melosh, 1984; Artemieva and Ivanov, 2004; Fritz et al., 2005). While the place of origin is not known for any of the Martian meteorites, Tooting crater with its target material comprised of basaltic lava flows (Scott and Tanaka, 1986), appears to be a strong candidate parent crater for at least some of these rocks.

Tooting crater is very large considering its very young age (thereby meeting the "large crater" criterion for the source of the SNCs; Vickery and Melosh, 1987) and, as we have shown in Section 2, the crater is likely to have an age <3 Ma and the pre-impact surface an age of ~240–375 Ma. We know of no other very young impact crater on Mars that is of comparable or larger size, although Tornabene et al. (2006) identified several smaller craters (Zumba [3.3 km], Gratteri [6.9 km], Tomini [7.4 km] and Zunil [10.1 km]) that could be the source for some of the Martian meteorites. The pre-existing terrain within which Tooting crater formed is seen from photogeologic mapping to be a sequence of young Amazonian-age lava flows (Scott and Tanaka, 1986). In addition, as we have shown (Figs. 22 and S39), the distribution of ejecta is non-symmetric, and Mouginis-Mark and Garbeil (2007) proposed that the crater was formed by an oblique impact, which numerical models suggest should promote the ejection of material into escape trajectories (Melosh, 1984). Large (>100 m diameter) secondary craters can be found in crater chains that point towards Tooting crater out to radial distances of at least 540 km from the rim crest, indicating that blocks were easily ejected to considerable distances during the impact event.

The basaltic shergottites ejected at ~2.8 Ma have crystallization ages that span a time period of ~170 Ma (~165 ± 11 Ma to 327 10 Ma) and are likely to have originated from a series of volcanic flows (McSween, 2008). A cluster of shergottites ejected ~1.2 Ma ago comprise volcanic rocks with crystallization ages that overlap but are mostly older than the basaltic shergottites, with crystallization ages ranging over ~185 Ma duration (~290 ± 40 Ma to 474 ± 11 Ma) implying that the target rocks contained multiple flows formed over a protracted period of time. In either case, the range of crystallization ages of the SNC rocks from either cluster indicates that they could come from the sequence of flows that comprise the target materials; there are no visible local vents for this flow sequence, and so the most plausible source of the flows is the southern flank of Olympus Mons volcano, which lies ~1350 km to the southeast. Based upon superposed crater distributions, Olympus Mons has been active over an extended period of Martian history that extends into the recent geologic past (Robbins et al., 2011; Hauber et al., 2011), and so it is reasonable for this volcano to be the source for the lava flows that subsequently provided the rocks that became the basaltic shergottites through the Tooting crater-forming impact event.

5.3. Implications for the recent distribution of sub-surface volatiles on Mars, and the thermal anomaly associated with a large impact crater

If Tooting crater did form ~2.9 Ma, then the abundant evidence for water within the target materials lends additional support to the idea of climate change on Mars. Present day observations from the gamma-ray spectrometer on the Mars Odyssey spacecraft (Feldman et al., 2004) show that this area of Mars has a relatively low water-equivalent inventory of hydrogen (~4%), and yet we see abundant evidence for water leaking out of the cavity walls as well as flowing on the surface of the ejecta layers. One possible explanation for this apparent conflict lies in the work of Head et al. (2003), who investigated the orbital forcing of climate in the past, and identified that ~3 Ma the mid-latitudes were in a glacial period that included accumulation and modification of ice. Thus it is quite possible that the target may have had a higher ice content at the time of crater formation than is present now.

Abramov and King (2005) conducted a numerical simulation of Tooting crater, investigating the effects of ground permeability and the presence of a crater lake. They found that host rock permeability was the main factor affecting fluid circulation and the lifetime of a hydrothermal system. They concluded that the hydrothermal system's lifetime could have been as long as ~65,000 years. Abramov and King (2005) argued that the highest temperatures are primarily focused around the central peak where temperatures and pressures are compatible with water's gaseous phase. Their model predicts that steam emission may have endured for almost 1000 years, with near-surface temperatures over 100 °C up to 6 km away from the crater's center.

It is possible to search for evidence of these thermal anomalies. If our interpretation of the mode of formation of the pitted material (i.e., the explosive release of gases from a hot, volatile-rich, layer of sediment) is correct, then the spatial distribution of pitted material (Fig. 9) would indicate high temperatures early in the crater's history over an area that includes much more of the crater floor and terraces. The potential existence of this hydrothermal system could have produced a wide variety of minerals, including some that could only have formed at temperatures in excess of 200 °C (Newsom, 1980; Newsom et al., 2001). Unfortunately, even though it is very young, Tooting crater is mantled in a layer of dust (Ruff and Christensen, 2002) that precludes orbital identification of minerals from Thermal Emission Spectrometer (TES) or CRISM data.

5.4. Terrestrial analogs

Our morphological observations may provide confirmation of processes inferred to have taken place in now-eroded terrestrial impact craters. For example, the 26 km diameter Ries crater, Germany, could present one of the best terrestrial analogs to fluidized ejecta craters on Mars. Ries crater is the largest terrestrial crater where substantial amounts of ejecta are preserved, and it has particular relevance to the interpretation of Tooting crater because the pre-impact target stratigraphy at Ries enables the ratio of primary crater ejecta to locally-derived materials to be determined for the ejecta blanket (Hörz et al., 1983). This ratio was found to decrease with increasing distance from the crater rim and suggests that the final phase of ejecta emplacement, probably analogous to the deposition of the layered ejecta materials of Tooting crater, was as a ground-hugging, highly turbulent, flow.

Hörz and Banholzer (1980) demonstrated that >99% of the entire Bunte Breccia at Ries, crater which constitutes the remnants of the ejecta blanket, is unshocked and demonstrates that the large-scale continuous ejecta deposits were emplaced as relatively cool masses essentially at ambient temperatures. Newsom et al. (1986) studied the suevite deposits at Ries crater, and found that there is a large number of chimney-like degassing pipes, apparently formed by high gas pressures in the hot (>500 °C) fluidized deposits immediately after deposition. The likely source of the gases was interpreted to be volatiles from the melted and shocked basement inclusions. The suevite groundmass at Ries crater (Osinski, 2004) may therefore be analogous to the volatile release inferred at Tooting crater, either to produce the pitted material, or to form the pits within the distal ramparts (Fig. S46).

The flow morphologies seen within the ejecta layers may also be analogs to certain terrestrial large landslides. The inner layer is characterized by this wavy pattern, while on the outer ejecta layers the sets of transverse ridges form chevron patterns. This suggests that the flow properties of Tooting ejecta changed with distance from the crater. Sets of closely-spaced transverse ridges and troughs within the ejecta layers (Fig. 19) are morphologically similar to features observed on terrestrial long run-out landslides (e.g., Shreve, 1966, 1968; Barnouin-Jha et al., 2005). These have been studied theoretically (Baloga and Bruno, 2005) and in the laboratory in both wet and dry granular materials (Schonfeld, 1996; Iverson, 1997; Prasad et al., 2000; Louge and Keating, 2001; Goldfarb et al., 2002; Forterre and Pouliquen, 2003), and it has been generally concluded that these features are rolling waves-like structures (also called "Kapitza waves"). Such structures are caused by instabilities produced by competition between inertia and gravity, as in classic fluids, but modified due to the specifics of the friction law of granular flows (Schonfeld, 1996; Iverson, 1997; Prasad et al., 2000; Forterre and Pouliquen, 2002, 2003).

Carpen and Brady (2002) investigated roll waves caused by gravitational instability in suspension flow and found that rapid granular flows (such as ejecta) are subject to the same instability as found in experiments of Forterre and Pouliquen (2003). Forterre and Pouliquen (2003) found that the wavelength of span-wise patterns (i.e., roll waves) on granular flows was of the order of three times the height of the layer (i.e., the emplaced ejecta). In a preliminary test of the predictive powers of this approach on ejecta of Tooting Crater, we measured the wavelength of its transverse ridges in several locations on its inner ejecta layer. We find that the thicknesses predicted from these measurements are similar to the nearby ejecta thickness values determined by Mouginis-Mark and Garbeil (2007) using MOLA (Fig. 17). Although the agreement is good, this is only a small sample. The agreement does suggest that little, if any, deflation of the ejecta deposit occurred after deposition, such as would be expected if it were heavily laden with water (e.g., see Major, 1997; Iverson and Denlinger, 2001).

5.5. Implications for the geology of older impact craters on Mars

The topographic data studied here are particularly relevant for understanding the original geometry of older impact craters on Mars. Our rim height measurements (Fig. 6) bring into question the value of using crater rim height as a reference level to measure crater depth, and for developing a single rim height to diameter ratio for impact craters on Mars. Prior to the availability of high resolution DEMs, single values of the rim height/crater diameter ratio were used to define the degradation state of individual crater on Mars (De Hon, 1981; Garvin et al., 2003; Forsberg-Taylor et al., 2004; Boyce et al., 2005; Stewart and Valiant, 2006), with the approximate relationship of $h = 0.02D^{0.84}$, where h is the rim height and D the crater diameter (both in kilometers). For Tooting crater, the Garvin et al. (2003) relationship would predict a rim height of ~340 m, which is equal to the lowest measured point on the rim, but only ~36% the highest point on the rim. Estimations of erosion rates have utilized the height of a crater rim. Arvidson et al. (1979) inspected Viking Lander images of craters seen in profile at the two lander sites to infer the degree of erosion, but there was insufficient information to measure the azimuthal variation in rim height for the craters imaged. Forsberg-Taylor et al. (2004) employed the average rim height of an impact crater as the starting point of their assessment of the degree of modification of the landform either by fluvial or eolian processes. Pike (1980), Stewart and Valiant (2006), Boyce et al. (2005, 2006), and Boyce and Garbeil (2007) used the rim height/crater diameter ratio for the freshest craters they could find to search for target strength differences between the lowlands and highlands of Mars. Our analysis shows that all of these prior studies of crater erosion would significantly under-estimate the pristine rim height, and thus under-estimate the extent of erosion.

The identification of ~240 m of structural uplift of the pre-impact surface (Fig. 10) and unconsolidated layers of ejecta as much as ~550 m thick on top of the uplifted target material suggests that the rims of Martian craters may erode at different rates over geologic time. We would expect that the unconsolidated ejecta would erode relatively quickly, as demonstrated by the deep erosion that already characterizes the rim crest (Fig. S20). Once the more coherent uplifted is exposed, the rim of the crater would probably erode more slowly. How this time-varying erosion rate might influence the rim height to crater diameter ratio remains to be determined, and will no doubt be influenced by the strength of the pre-impact target. However, searching for unconsolidated material in the wall of a crater cavity may represent a new criterion for saying that one crater is younger than another of a similar size.

Our measurements of the central peak (Fig. 5) imply that, if the floor was at an elevation of ~100 m below the mean datum (~760 m below the mean rim elevation), then the central peak would be entirely buried. Thus, if Tooting crater was an older, more degraded, crater with a depth/diameter ratio of ~0.026, then the peak would be entirely buried. Furthermore, infilling the southern floor of the

crater cavity with only ~200 m of material (thereby creating a crater with a depth/diameter ratio of 0.06) would bury all evidence of the fractured material (Fig. S11) on the crater floor. These observations imply that many of the earlier Viking Orbiter-based interpretations of the geometric properties of Martian craters (Wood et al., 1978; Hale, 1983; Barlow and Bradley, 1990) were influenced by the inability to identify truly fresh impact craters; we infer that many craters studied using Viking Orbiter images have a significant volume of fill within the interior of the crater, and are now significantly shallower than at the time that they formed.

Considering Tooting crater as the very fresh end-member example of multi-layered ejecta (MLE) craters, it appears highly likely that we can expect that many older craters would once have had proportionally larger central peaks, a greater cavity depth, and a significant amount of impact melt. However, it is not clear if the crater is a good analog to fresh (or old) double-layered ejecta (DLE) craters (Barlow et al., 2000). There are several key differences that can be identified for the freshest DLE craters:

(1) There is a lack of pitted material on the floor of most DLE craters. We speculate that such material may have been formed at DLE craters, but that the last phase of ejecta emplacement, which produced the outer ejecta layer (Mouginis-Mark, 1981), swept away the pitted material.
(2) The morphology of the central peaks within DLEs is different, with no indication of layering with DLE craters. Where present, the DLE peaks are often smaller than those observed within SLE or MLE craters.
(3) Boyce and Mouginis-Mark (2006) describe several topographic attributes of DLE crater ejecta blankets and showed that DLEs lack prominent ramparts, and have a "moat" between the crater rim and the edge of the inner ejecta layer. Thus the radial distribution of ejecta thickness (Figs. 17 and S39) may be different from that typically seen at DLE craters.
(4) The exterior rim of DLE craters such as Bacolor has failed in discrete segments that have then been "consumed" during radial flow away from crater. The rim material of Tooting crater (Figs. 10 and 18) is wider, thicker, and appears to have been emplaced with more volatiles than was typical for DLE craters (Boyce and Mouginis-Mark, 2006).
(5) Unlike the morphology of Tooting crater, there are prominent radial features on the two ejecta layers of Martian DLE craters (Boyce and Mouginis-Mark, 2006). These radial features are similar to the two zones in the area devastated by the gas-driven lateral blast of the 1980 eruption at Mount St. Helens (Kieffer, 1981; Kieffer and Sturtevant, 1988). These striations are not visible within the ejecta layers of Tooting crater (Fig. 19). However, for DLE craters, the straight grooves on the inner ejecta layer may have been produced by scouring associated with a supersonic surge of ejecta. The speed of ejecta flow across the ground may, therefore, be different for MLE and DLE craters.

Finally, the abundant evidence for volatiles within the crater cavity, and the inclusion of water within the ejecta layers (Figs. S41 and S42) at the time of their emplacement, argues strongly for the over-riding control of volatiles in the fluidization of the ejecta layers (Carr et al., 1977; Mouginis-Mark, 1979). The lack of morphologic evidence for atmospheric winnowing of ejecta and the presence of water release from the distal margins of the ejecta layers (Fig. S43) are inconsistent with the model of atmospheric entrainment within the ejecta blanket (Schultz and Gault, 1979; Barnouin-Jha and Schultz, 1998) as the cause of ejecta fluidization. If Tooting crater can indeed be taken as the archetype for older fluidized ejecta craters on Mars, then the implication is that the ejecta blankets can be interpreted in terms of spatial and temporal variations of volatiles on the planet (Mouginis-Mark, 1979; Barlow and Perez, 2003).

6. Conclusions

Tooting crater is a remarkably well preserved ~27 km diameter impact crater on Mars. By virtue of the excellent very high resolution image data that have been collected for the crater, it is possible to identify a wide diversity of landforms that have previously not been documented for craters on Mars. Topographic data offer valuable insights into the distribution of ejecta, the thickness of the ejecta layers, the geometry of the crater cavity, height of the central peak, and the amount of structural uplift of the pre-existing target material. The occurrence of units that appear to be impact melt on the rim of the crater, as well as ample evidence for the release of water from the interior and exterior of the crater cavity, offer unique insights into the importance of pre-existing volatiles in the target at the time of impact. Dewatering of the ejecta layers lends credibility to the notion that the lobate ejecta layers around this and, by inference, other MLE craters on Mars were fluidized by water or ice in the target, rather than by the atmosphere. Counts of superposed small impact craters on the ejecta layers indicate a very young age that may be <3 million years, raising the intriguing possibility that Tooting crater is the source of some of the SNC meteorites and thus providing a potential age of the Amazonian lava flows that comprised the target of ~1.3 billion years.

Acknowledgments

This Invited Review was solicited by Associate Editor Klaus Keil, who provided continuous encouragement to the authors to write this contribution over the many years of its gestation. We thank Philip Christensen and Alfred McEwen, and the THEMIS and HiRISE imaging teams, for the collection of many of the images used here. Aisha Morris and Harold Garbeil contributed to earlier discussions on the geology of Tooting crater, and we acknowledge the comments made by two anonymous reviewers. Harold Garbeil produced the digital elevation models used in this study. This research was conducted under funding from the Planetary Geology and Geophysics Program, under NASA grant NNX06AC61G. This is HIGP Publication 1918, and SOEST Contribution 8540.

Appendix A. Supplementary data

Supplementary data associated with this article can be found, in the online version, at doi:10.1016/j.chemer.2011.12.001.

References

Abramov, O., King, D.A., 2005. Impact-induced hydrothermal activity early Mars. J. Geophys. Res. 110, E12S09, doi:10.1029/2005JE002453.
Artemieva, N.A., Ivanov, B.A., 2004. Launch of Martian meteorites in oblique impacts. Icarus 171, 84–101.
Arvidson, R.E., Guiness, E.A., Lee, S., 1979. Differential Aeolian redistribution rates on Mars. Nature 278, 533–535.
Baloga, S.M., Bruno, B.C., 2005. Origin of transverse ridges on the surfaces of catastrophic mass flow deposits on the Earth and Mars. J. Geophys. Res. 110 (E5), doi:10.1029/2004JE002381.
Baloga, S.M., Fagents, S.A., Mouginis-Mark, P.J., 2005. The emplacement of Martian rampart crater deposits. J. Geophys. Res. 110, E10001, doi:10.1029/2004JE002338.
Baratoux, D., Mangold, N., Pinet, P., Costard, F., 2005. Properties of lobate ejecta in Syrtis Major, Mars: implications for the mechanisms of formation. J. Geophys. Res. 110, E04011, doi:10.1029/2004JE002314.
Baratoux, D., Delacourt, C., Allemand, P., 2002. An instability mechanism in the formation of the Martian lobate craters and the implications for the rheology of ejecta. Geophys. Res. Lett. 29 (8), 1210, doi:10.1029/2001GL013779.
Baratoux, D., Pinet, P., Gendrin, A., Kanner, L., Mustard, J., Daydou, Y., Vaucher, J., Bibring, J.-P., 2007. Mineralogical structure of the subsurface of Syrtis Major from OMEGA observations of lobate ejecta blankets. J. Geophys. Res. 112, E08S05, doi:10.1029/2007JE002890.

Barlow, N.G., Boyce, J.M., Costard, F.M., Craddock, R.A., Garvin, J.B., Sakimoto, S.E.H., Kuzmin, R.O., Roddy, D.J., Soderblom, L.A., 2000. Standardizing the nomenclature of Martian impact crater ejecta morphologies. J. Geophys. Res. 105, 26733–26738.
Barlow, N.G., 1994. Sinuosity of Martian rampart ejecta deposits. J. Geophys. Res. 99, 10927–10935.
Barlow, N.G., Bradley, T.L., 1990. Martian impact craters: correlations of ejecta and interior morphologies with diameter, latitude, and terrain. Icarus 87, 156–179.
Barlow, N.G., Perez, C.B., 2003. Martian impact crater ejecta morphologies as indicators of the distribution of subsurface volatiles. J. Geophys. Res. 108, E8, doi:10.1029/2002JE002036.
Barnhart, C.J., Nimmo, F., Travis, B.J., 2010. Martian post-impact hydrothermal systems incorporating freezing. Icarus 208, 101–117.
Barnouin-Jha, O.S., Schultz, P.H., 1996. Ejecta entrainment by impact-generated ring vortices: theory and experiments. J. Geophys. Res. 101, 21099–21115.
Barnouin-Jha, O.S., Schultz, P.H., 1998. Lobateness of impact ejecta deposits from atmospheric interactions. J. Geophys. Res. 103, 25739–25756.
Barnouin-Jha, O.S., Baloga, S., Glaze, L., 2005. Comparing landslides to fluidized crater ejecta on Mars. J. Geophys. Res. 110, E04010, doi:10.1029/2003JE002214.
Black, B.A., Stewart, S.T., 2008. Excess ejecta craters record episodic ice-rich layers at middle latitudes on Mars. J. Geophys. Res. 113, E02015, doi:10/1029/2007JE002888.
Blewett, D.T., et al., 2011. Hollows on Mercury: MESSENGER evidence for geologically recent volatile-related activity. Science 333, 1856–1859.
Borgia, A., Burr, J., Montero, W., Morales, L.D., Alvarado, G.E., 1990. Fault-propagation folds induced by gravitational failure and slumping of the Central Costa Rica volcanic range: implications for large terrestrial and Martian volcanic edifices. J. Geophys. Res. 95, 14357–14382.
Boyce, J.M., Mouginis-Mark, P.J., 2006. Martian craters viewed by the THEMIS instrument: double-layered ejecta craters. J. Geophys. Res. 111, E10005, doi:10.1029/2005JE002638.
Boyce, J.M., Garbeil, H., 2007. Geometric relationships of pristine Martian complex impact craters, and their implications to Mars geologic history. Geophys. Res. Lett. 34, doi:10.1029/2007GL029731.
Boyce, J.M., Mouginis-Mark, P.J., Garbeil, H., 2005. Ancient oceans in the lowlands of Mars: Evidence from impact crater depth/diameter relationships. J. Geophys. Res. 110 (E3), doi:10.1029/2004JE002328.
Boyce, J.M., Mouginis-Mark, P.J., Garbeil, H., Tornabene, L., 2006. Deep impact craters in the Isidis and southwestern Utopia region of Mars: high target strength as a possible cause. Geophys. Res. Lett., L06202, doi:10.1029/2005GL024462.
Boyce, J.M., Barlow, N., Mouginis-Mark, P.J., Stewart, S., 2010. Ganymede rampart craters: their implications for fluidized ejecta emplacement. Meteorit. Planet. Sci. 45 (4), 638–661.
Bray, V.J., et al., 2010. New insight into lunar impact melt mobility from LRO camera. Geophys. Res. Lett. 37, L21202, doi:10.1029/2010GL044666.
Byrne, S., et al., 2009. Distribution of mid-latitude ground ice on Mars from new impact craters. Science 325, 1674–1676.
Cahill, J.T.S., Lucey, P.G., Wieczorek, M.A., 2009. Compositional variations of the lunar crust: results for radiative transfer modeling of central peak spectra. J. Geophys. Res. 114, E09001, doi:10.1029/2008JE003282.
Calef, F.J., Herrick, R.R., Sharpton, V.L., 2009. Geomorphic analysis of small rayed craters on Mars: examining primary versus secondary impacts. J. Geophys. Res. 114, E10007, doi:10.1029/2008JE003283.
Campbell, B.A., Carter, L., Phillips, R., Plaut, J., Putzig, N., Safaeinili, A., Seu, R., Biccari, D., Egan, A., Orosei, R., 2008. SHARAD radar sounding of the Vastitas Borealis Formation in Amazonis Planitia. J. Geophys. Res. 113, E12010, doi:10.1029/2008JE003177.
Carpen, I., Brady, J., 2002. Gravitational instability in suspension flow. J. Fluid Mech. 472, 201–210.
Carr, M.H., Crumpler, L., Cutts, J., Greeley, R., Guest, J., Masursky, H., 1977. Martian impact craters and emplacement of ejecta by surface flow. J. Geophys. Res. 82, 4055–4065.
Cintala, M.J., Grieve, R.A.F., 1998. Scaling impact melting and crater dimensions: implications for the lunar cratering record. Meteorit. Planet. Sci. 33, 889–912.
De Hon, R., 1981. Martian volcanic materials: preliminary thickness estimates in the Eastern Tharsis region. J. Geophys. Res. 87 (B12), 9821–9828.
Denlinger, R.P., Iverson, R.M., 2001. Flow of variably fluidized granular masses across three-dimensional terrain: 2. Numerical predictions and experimental tests. J. Geophys. Res. 106 (B1), 553–566.
Feldman, W.C., et al., 2004. Global distribution of near-surface hydrogran on Mars. J. Geophys. Res. 109, E09006, doi:10.1029/2003JE002160.
Ferriere, L., Koeberl, C., Ivanov, B.A., Reimold, W.U., 2008. Shock metamorphism of Bosumtwi impact crater tocks, shock attenuation, and uplift formation. Science 322, 1678–1681.
Fink, J.H., 1980. Surface folding and viscosity of rhyolite flows. Geology 8, 250–254.
Forsberg-Taylor, N.K., Howard, A.D., Craddock, R.A., 2004. Crater degradation in the Martian highlands: morphometric analysis of the Sinus Sabaeus region and simulation modeling suggest fluvial processes. J. Geophys. Res. 109, E05002, doi:10.1029/2004JE002242.
Forterre, Y., Pouliquen, O., 2002. Stability analysis of rapid granular chute flows: formation of longitudinal vortices. J. Fluid Mech. 467, 361–387.
Forterre, Y., Pouliquen, O., 2003. Long-surface-wave instability in dense granular flows. J. Fluid Mech. 486, 21–50.
Fritz, J., Artemieva, N., Greshake, A., 2005. Ejection of Martian meteorites. Meteorit. Planet. Sci. 40, 1393–1411.
Garvin, J.B., Frawley, J.J., 1998. Geometric properties of Martian impact craters: preliminary results from Mars Orbiter Laser Altimeter. Geophys. Res. Lett. 25, 4405–4408.
Garvin, J.B., Sakimoto, S.E.H., Frawley, J.J., 2003. Craters on Mars: global geometric properties from gridded MOLA topography. In: Sixth Int. Conf. Mars, (Abstract #3277).
Gault, D.E., Greeley, R., 1978. Exploratory experiments of impact craters formed in viscous targets: analogs for Martian rampart craters. Icarus 34, 486–495.
Gilmore, M.S., Phillips, E.L., 2002. Role of aquicludes in formation of Martian gullies. Geology 30 (12), 1107–1110.
Goldfarb, D., Glasser, B., Shinbrot, T., 2002. Shear instabilities in granular flows. Nature 415, 302–305.
Greeley, R., Fink, J., Gault, D.E., Snyder, D.B., Guest, J.E., Schultz, P., 1980. Impact cratering in viscous targets: laboratory experiments. In: Proc. Lunar Planet. Sci. Conf. 11th, pp. 2075–2097.
Guest, J.E., 1973. Stratigraphy of ejecta from the lunar crater Aristarchus. Geol. Soc. Am. Bull. 84, 2873–2894.
Guest, J.E., Murray, J.B., 1971. A large scale pattern associated with the ejecta blanket and rays of Copernicus. Moon 3, 326–336.
Hale, W.S., 1983. Central structures in Martian impact craters: morphology, morphometry, and implications for subsurface volatile distributions. In: Lunar Planet. Sci. Conf. XIV, pp. 273–274 (Abstract).
Hamilton, V.E., Christensen, P.R., McSween, H.Y., Bandfield, J.L., 2003. Searching for the source regions of Martian meteorites using MGS TES: integrating Martian meteorites into the global distribution of igneous materials on Mars. Meteorit. Planet. Sci. 38, 871–885.
Hartmann, W.K., 2005. Martian cratering: 8. Isochron refinement and the history of Martian geologic activity. Icarus 174, 294–320.
Hartmann, W.K., Neukum, G., 2001. Crater chronology and the evolution of Mars. In: Kallenbach, R., et al. (Eds.), Chronology and Evolution of Mars. Kluwer, Dordrecht, Germany, pp. 165–194.
Hartmann, W.K., Quantin, C., Werner, S.C., Popova, O., 2010. Do young Martian craters have ages consistent with the crater count system? Icarus 208, 621–635.
Hauber, E., Broz, P., Jagert, F., Jodlowski, P., Platz, T., 2011. Very recent and wide-spread basaltic volcanism on Mars. Geophys. Res. Lett. 38, L10201, doi:10.1029/2011GL047310.
Head, J.W., Roth, R.,1976. Mars pedestal crater escarpments: evidence for ejecta-related emplacement. In: Papers Presented to the Symposium on Planetary Cratering Mechanics. Lunar Sci. Inst., Houston, Texas, pp. 50–52.
Head, J.W., Mustard, J.F., Kreslavsky, M.A., Milliken, R.E., Marchant, D.R., 2003. Recent ice ages on Mars. Nature 426, 797–802.
Heather, D.J., Dunkin, S.K., 2003. Geology and stratigraphy of King crater, lunar far side. Icarus 163, 307–329.
Horner, V.M., Greeley, R., 1987. Effects of elevation and ridged plains thicknesses on Martian crater ejecta morphology. Proc. Lunar Planet. Sci. Conf. 17th, Part 2. J. Geophys. Res. 92 (Suppl.), E561–E569.
Hörz, F., Ostertag, R., Rainey, D.A., 1983. Bunte breccia of Ries: continuous deposits of large impact craters. Rev. Geophys. Space Phys. 21, 1667–1725.
Hörz, F., Banholzer, G.S., 1980. Deep seated target materials in the continuous deposits of the Ries Crater, Germany. In: Papike, J.J., Merrill, R.B. (Eds.), Proc. Conf. Lunar Highlands Crust. , pp. 211–231.
Howard, K.A., 1975. Geologic Map of the Crater Copernicus. U.S. Geological Survey Map I-840.
Howard, K.A., Wilshire, H.G., 1975. Flows of impact melt at lunar craters. J. Res. U. S. Geol. Survey 3, 237–251.
Ivanov, B.A., 1996. Spread of ejecta from impact craters and the possibility of estimating the volatile content of the Martian crust. Sol. Sys. Res. 30 (1), 36–50.
Ivanov, B., 2001. Mars/Moon cratering rate ratio estimates. Space Sci. Rev. 96, 87–104.
Iverson, R.M., Denlinger, R.P., 2001. Flow of variably fluidized granular masses across three-dimensional terrain: 1. Coulomb mixture theory. J. Geophys. Res. 106 (B1), 537–552.
Iverson, R.M., 1997. The physics of debris flows. Rev. Geophys. 35, 245–296.
Jones, A.P., McEwen, A.S., Tornabene, L.L., Baker, V.R., Melosh, H.J., Berman, D.C., 2011. A geomorphic analysis of Hale crater, Mars: the effects of impact into ice-rich crust. Icarus 211, 259–272.
Kenkmann, T., Schonian, F., 2006. Ries and Chicxulub: impact craters on Earth provide insights for Martian ejecta blankets. Meteorit. Planet. Sci. 41, 1587–1603.
Kieffer, S.W., 1981. Fluid dynamics of the May 18, 1980 blast at Mount St Helens. In: Lipman, P.W., Mullineaux, D.R. (Eds.), The 1980 Eruption of Mount St Helens, Washington. U.S. Geol. Survey, Prof. Paper 1250, pp. 379–400.
Kieffer, S.W., Simonds, C.H., 1980. The role of volatiles and lithology in the impact cratering process. Rev. Geophys. Space Phys. 18, 143–181.
Kieffer, S.W., Sturtevant, B., 1988. Erosional furrows formed during the lateral blast at Mount St. Helens, May 18, 1980. J. Geophys. Res. 93 (B12), 14793–14816.
Kring, D.A., Gleason, J.D., Swindle, T.D., Nishiizumi, K., Caffee, M.W., Hill, D.H., Jull, A.J.T., Boynton, W.V., 2003. Composition of the first bulk melt sample from a volcanic region of Mars: Queen Alexandra Range 94201. Meteorit. Planet. Sci. 38, 1833–1848.
Laity, J.E., Malin, M.C., 1985. Sapping processes and the development of theater-headed valley networks on the Colorado Plateau. Geol. Soc. Am. Bull. 96, 203–217.
Lamb, M., Howard, A.D., Johnson, J., Whipple, K.X., Dietrich, W.E., Perron, J.T., 2006. Can springs cut canyons into rock? J. Geophys. Res. 111, E07002, doi:10.1029/2005JE002663.

Lang, N.P., Tornabene, L.L., McSween, H.Y., Christensen, P.R., 2009. Tharsis-sourced relatively dust-free lavas and their possible relationship to Martian meteorites. J. Volcanol. Geotherm. Res. 185, 103–115.
Lanza, N.L., Meyer, G.A., Okubo, C.H., Newsom, H.E., Wiens, R.C., 2010. Evidence for debris flow gully formation initiated by shallow subsurface water on Mars. Icarus 205, 103–112.
Louge, M.Y., Keating, S.C., 2001. On dense granular flows down flat frictional inclines. Phys. Fluids 13, 1213–1233.
Major, J.J., 1997. Depositional processes in large-scale debris-flow experiments. J. Geol. 105, 345–366.
Malin, M.C., Edgett, K.S., 2000. Evidence for recent groundwater seepage and surface runoff on Mars. Science 288, 2330–2335.
McEwen, A.S., et al., 2007. A closer look at water-related geologic activity on Mars. Science 317, 1706–1709.
McEwen, A.S., Ojha, L., Dundas, C.M., Mattson, S.S., Byrne, S., Wray, J.J., Cull, S.C., Murchie, S.L., Thomas, N., Gulick, V.C., 2011. Seasonal flows on warm Martian slopes. Science 333, 740–743.
McEwen, A.S., Preblich, B.S., Turtle, E.P., Artemieva, N.A., Golombek, M.P., Hurst, M., Kirk, R.L., Burr, D.M., Christensen, P., 2005. The rayed crater Zunil and interpretations of small impact craters on Mars. Icarus 176, 351–381.
McGovern, P.J., Smith, J.R., Morgan, J.K., Bulmer, M.H., 2004. Olympus Mons aureole deposits: new evidence for a flank failure origin. J. Geophys. Res. 109, E08008, doi:10.1029/2004JE002258.
McSwaveney, M., 1978. Sherman Glacier rock avalanche, Alaska, U.S.A. In: Voight, B. (Ed.), Rockslides and Avalanches: 1. Natural Phenomena, Development of Geotechnical Engineering, vol. 14A, pp. 197–258.
McSween, H.Y., Eisenhour, D.D., Taylor, L.A., Wadhwa, M., Crozaz, G., 1996. QUE 94201 shergottite: crystallization of a Martian basaltic magma. Geochim. Cosmochim. Acta 60, 4563–4569.
McSween, H.Y., 2008. Martian meteorites as crustal samples. In: Bell III, J.F. (Ed.), The Martian Surface: Composition, Mineralogy, and Physical Properties. Cambridge University Press, pp. 383–395.
Mellon, M.T., et al., 2009. Ground ice at the Phoenix landing site: stability state and origin. J. Geophys. Res. 114, E00E07, doi:10.1029/2009JE003417.
Mellon, M.T., Jakosky, B.M., Kieffer, H.H., Christensen, P.R., 2000. High-resolution thermal inertia mapping from the Mars Global Surveyor Thermal Emission Spectrometer. Icarus 148, 437–455.
Melosh, J.J., 1984. Impact ejection, spallation, and the origin of meteorites. Icarus 59, 234–260.
Melosh, H.J., 1989. Impact Cratering. Oxford University Press, New York, 245 pp.
Morgan, G.A., Head, J.W., Marchant, D.R., 2009. Lineated valley fill (LVF) and lobate debris aprons (LDA) in the Deuteronilus Mensae northern dichotomy boundary region, Mars: constraints on the extent, age and episodic. Icarus 202, 22–38.
Morris, A.R., Mouginis-Mark, P.J., Garbeil, H., 2010. Possible impact melt and debris flows at Tooting crater, Mars. Icarus 209, 369–389.
Mouginis-Mark, P.J., 1978. Morphology of Martian rampart craters. Nature 272, 691–694.
Mouginis-Mark, P.J., 1979. Martian fluidized crater morphology: variations with crater size, latitude, altitude and target material. J. Geophys. Res. 84, 8011–8022.
Mouginis-Mark, P., 1981. Ejecta emplacement and modes of formation of Martian fluidized ejecta craters. Icarus 45, 60–76.
Mouginis-Mark, P.J., 1987. Water or ice in the Martian regolith? Clues from rampart craters seen at very high resolution. Icarus 71, 268–286.
Mouginis-Mark, P.J. 1:200,000 Geologic map of Tooting crater, Mars. U. S. Geological Survey Miscellaneous Map Series, submitted for publication.
Mouginis-Mark, P.J., Baloga, S.M., 2006. Morphology and geometry of the distal ramparts of Martian impact craters. Meteorit. Planet. Sci. 41, 1469–1482.
Mouginis-Mark, P.J., Boyce, J.M., Hamilton, V.E., Anderson, F.S., 2003. A very young, large, impact crater on Mars. In: Int. Mars Conf. VI, (Abstract #3004).
Mouginis-Mark, P.J., Garbeil, H., 2007. Crater geometry and ejecta thickness of the Martian impact crater Tooting. Meteorit. Planet. Sci. 42, 1615–1625.
Mouginis-Mark, P.J., McCoy, T.J., Taylor, G.J., Keil, K., 1992. Martian parent craters for the SNC meteorites. J. Geophys. Res. 97, 10213–10225.
Mouginis-Mark, P.J., Rowland, S.K., 2008. Lava flows at Arsia Mons, Mars: insights from a graben imaged by HiRISE. Icarus 198, 27–36.
Newsom, H.E., Hagerty, J.J., Thorsos, I.E., 2001. Location and sampling of aqueous and hydrothermal deposits in Martian impact craters. Astrobiology 1, 78–88.
Newsom, H.E., 1980. Hydrothermal alteration of impact melt sheets with implications for Mars. Icarus 44, 207–216.
Newsom, H.E., Graup, G., Sewards, T., Keil, K., 1986. Fluidization and hydrothermal alteration of the suevite deposits at the Ries crater, West Germany, and implications for Mars. Proc. 17th Lunar Planet. Sci. Conf., pt. 1. J. Geophys. Res. 91, E239–E251.
Oberbeck, V.R., Morrison, R.H., 1973. On the formation of lunar herringbone pattern. Lunar Sci. Conf. Proc. 4, 107–123.
Osinski, G.R., 2004. Impact melt rocks from the Ries structure, Germany: an origin as impact melt flows. Earth Planet. Sci. Lett. 226, 529–543.
Osinski, G.R., 2006. Effect of volatiles and target lithology on the generation and emplacement of impact crater fill and ejecta deposits on Mars. Meteorit. Planet. Sci. 41, 1571–1586.
Osinski, G.R., Grieve, R.A.F., Spay, J.G., 2004. The nature of the groundmass of surficial suevites from the Ries impact structure, Germany, and constraints on its origin. Meteorit. Planet. Sci. 39, 1655–1684.
Osinski, G.R., Grieve, R.A.F., Collins, G.S., Marion, C., Sylvester, P., 2008. The effect of target lithology on the products of impact melting. Meteorit. Planet. Sci. 43, 1939–1954.
Pieters, C.M., 1982. Copernicus crater central peak: lunar mountain of unique composition. Science 215, 59–61.
Pike, R.J., 1980. Control of crater morphology by gravity and target type: Mars, Earth, Moon. In: Proc. Lunar Planet. Sci. Conf. 11th, pp. 2159–2189.
Pouliquen, O., Vallance, J.W., 1999. Segregation induced instabilities of granular fronts. Chaos 9, 621–630.
Prasad, S.N., Pal, D., Romkens, M., 2000. Wave formation on a shallow layer of flowing grains. J. Fluid Mech. 413, 89–110.
Preblich, B.S., McEwen, A.S., Studer, D.M., 2007. Mapping rays and secondary craters from the Martian crater Zunil. J. Geophys. Res. 112, E05006, doi:10.1029/2006JE002817.
Rathbun, J.A., Squyres, S.W., 2002. Hydrothermal systems associated with Martian impact craters. Icarus 157, 362–372.
Robbins, S.J., Di Achille, G., Hynek, B.M., 2011. The volcanic history of Mars: high-resolution crater-based studies of the calderas of 20 volcanoes. Icarus 211, 1179–1203.
Ruff, S.W., Christensen, P.R., 2002. Bright and dark regions on Mars: particle size and mineralogical characteristics based on Thermal Emission Spectrometer data. J. Geophys. Res. 107, E12, doi:10.1029/2001JE001580.
Savage, S.B., Hutter, K., 1989. The motion of a finite mass of granular material down a rough incline. J. Fluid Mech. 199, 177–215.
Schonfeld, B., 1996. Roll waves in granular flows and debris flows. Master's thesis. Montreal, Canada, McGill University, p. 160.
Schultz, P.H., 1992. Atmospheric effects on ejecta emplacement. J. Geophys. Res. 97, 11623–11662.
Schultz, P.H., Gault, D.E., 1979. Atmospheric effects on Martian ejecta emplacement. J. Geophys. Res. 84, 7669–7687.
Scott, D.H., Tanaka, K.L., 1986. Geologic map of the western equatorial region of Mars, 1:15,000,000. U. S. Geological Survey Miscellaneous Investigation Series Map I-1082-A.
Shreve, R.L., 1966. Sherman landslide. The Great Alaskan Quake of 1964, Part A: Hydrology, vol. 1603. Natl. Acad. Sci. Publ, pp. 395–4012.
Shreve, R.L., 1968. The Blackhawk Landslide. Geol. Soc. Am. Spec. Paper 108, 47 pp.
Smith, D.E., et al., 1999. The global topography of Mars and implications for surface evolution. Science 284, 1495–1503.
Stewart, S.T., Valiant, G.J., 2006. Martian subsurface properties and crater formation processes inferred from fresh impact crater geometries. Meteorit. Planet. Sci. 41 (10), 1509–1537.
Strom, R.G., Fielder, G., 1971. Multiphase eruptions associated with the craters Tycho and Aristarchus. In: Fielder, G. (Ed.), Geology and Physics of the Moon. Elsevier Press, Amsterdam, pp. 55–92.
Theilig, E., Greeley, R., 1986. Lava flows on Mars: analysis of small surface features and comparisons with terrestrial analogs. J. Geophys. Res. 90, E193–E206.
Tornabene, L.L., Moersch, J.E., McSween Jr., H.Y., McEwen, A.S., Piatek, J.L., Milam, K.A., Christensen, P.R., 2006. Identification of large (2–10 km) rayed craters on Mars in THEMIS thermal infrared images: implications for possible Martian meteorite source regions. J. Geophys. Res. 111, doi:10.1029/2005JE002600.
Tornabene, L.L., McEwen, A.S., Osinski, G.R., Mouginis-Mark, P.J., Boyce, J.M., Williams, R.M.E., Wray, J.J., Grant, J.A., HiRISE Team, 2007. Impact melting and the role of subsurface volatiles: implications for the formation of valley networks and phyllosilicate-rich lithologies on early Mars. In: Seventh International Conference on Mars. Lunar Planet. Sci. Inst. Contribution #1353, Pasadena, CA.
Treiman, A.H., 1995. S ≠ NC: multiple source areas for Martian meteorites. J. Geophys. Res. 100 (E3), 5329–5340.
Vickery, A.M., Melosh, H.J., 1987. The large crater origin of SNC meteorites. Science 237, 738–743.
Wieczorek, M.A., Zuber, M.T., 2001. The composition and origin of the lunar crust: constraints from central peaks and crustal thickness modeling. Geophys. Res. Lett. 28, 4023–4026, doi:10.1029/2001GL012918.
Williams, R.M.E., Malin, M.C., 2008. Sub-kilometer fans in Mojave crater, Mars. Icarus 198, 365–383.
Williams, S.H., Zimbelman, J.R., 1994. "White Rock": an eroded Martian lacustrine deposit(?). Geology 22, 107–110.
Wood, C.A., Ashwal, L.D., 1981. SNC meteorites: igneous rocks from Mars? In: Proceedings, 12th Lunar Planet. Sci. Conf, pp. 1359–1375.
Wood, C.A., Head, J.W., Cintala, M.J., 1978. Interior morphology of fresh Martian craters: the effects of target characteristics. In: Proc. Lunar Planet. Sci. Conf. 9th, pp. 3691–3709.
Woronow, A., 1981. Preflow stresses in Martian rampart ejecta blankets: a means of estimating the water content. Icarus 45, 320–330.